AIAA Aviation Forum and ASCEND co-located Conference Proceedings
21 - 25 July 2025, Las Vegas, Nevada
AIAA AVIATION FORUM AND ASCEND 2025

10.2514/6.2025-3550

Integrated Guidance and Control of Quasi-Equilibrium Hypersonic Gliding Using Model Predictive Control

Diganta Bhattacharjee*, Sam A. Jaeger† and Maziar S. Hemati‡
University of Minnesota, Minneapolis, MN 55455, USA

This paper presents a guidance and control framework for hypersonic glide vehicles (HGVs) in atmospheric re-entry missions, wherein the guidance is designed in conjunction with the flight controls to synergistically integrate mission requirements with capabilities of the airframe, resulting in a comprehensive design and analysis architecture. Three-dimensional motion of the vehicle—executing a constant dynamic pressure glide subject to quasi-equilibrium conditions—is considered under the assumption that bank angle can be modulated directly. The proposed guidance subsystem computes trajectories that enable gliding at a specified dynamic pressure despite perturbations caused by initialization errors and/or external disturbances during flight. Inclusion of bank angle extends the feasible trajectory design space, thereby promoting flexibility of operation and providing the option to include additional mission-related requirements. The trajectory computation is online and inherently coupled with the flight controller which synthesizes the control inputs—stabilator deflection and bank angle—for trajectory tracking using a linear time-varying model predictive control design that embeds box constraints on the control input magnitudes. Closed-loop simulations of a generic HGV are used to demonstrate robust tracking of trajectories subject to plant-model mismatch and initialization errors. Load factors and heat fluxes are analyzed along simulated closed-loop trajectories, with the former converging to a constant value after transient oscillations initially and the latter showcasing an approximately monotonic decrease throughout.

I. Introduction

Autonomous and semi-autonomous flight technology suitable for hypersonic gliding and air-breathing vehicles have gained significant attention in recent times due to a plethora of civilian and military applications. Research efforts have largely been focused on developing trajectory generation (i.e., guidance [1]) and flight control architectures capable of guaranteeing vehicle and/or mission performance subject to modeling and parametric uncertainties [2–10], external disturbances [11–13], measurement inaccuracies [4, 7, 14], trajectory initialization errors [2, 3, 6], airframe and operational constraints [15–27], and more. Recent advances in multi-disciplinary design analysis and optimization (MDAO) promise to greatly aid hypersonic system development by providing tools that can effectively capture multi-physics and multi-disciplinary phenomena inherent to hypersonic flight and allow for various couplings between subsystems to be efficiently captured in a system-level optimization framework [28–30].

The current study broadly focuses on the coupling between trajectory generation/optimization and control synthesis, which can be regarded as a sub-problem within an extensive, system-wide MDAO. The capability to rapidly generate/simulate moderate-to-high fidelity hypersonic trajectories and associated flight controls is useful as it allows for design optimization with appropriate aero-thermal, structural and control constraints, which reflect physical limitations of the airframe subject to hypersonic flight conditions. To this end, one could consider a two-loop architecture comprising a guidance subsystem in the outer-loop and a control subsystem or controller in the inner-loop [31]. The guidance subsystem generates trajectories while remaining agnostic to the inner-loop control design. The controller then synthesizes flight controls required to fly those trajectories. Foundational principles behind these architectures are similar to the separation principle invoked for estimation-based feedback control designs [32] and typically involve time-scale separation arguments. As a result of the inherent decoupling, it is possible for the guidance subsystem to compute a trajectory that is infeasible to track using the available flight controls. Even if feasible, performance of the overall architecture could be unsatisfactory, possibly leading to instability in worst-case scenarios.

*Postdoctoral Research Associate, Department of Aerospace Engineering and Mechanics, AIAA Member. Email: dbhattac@umn.edu
†Graduate Student, Department of Aerospace Engineering and Mechanics, AIAA Student Member. Email: jaege246@umn.edu
‡Associate Professor, Department of Aerospace Engineering and Mechanics, AIAA Associate Fellow. Email: mhemati@umn.edu

Constructing a comprehensive architecture explicitly accounting for the coupling between trajectory and flight controls, often termed an integrated guidance and control (IGC) framework, holds the potential to remedy these above-mentioned issues [31]. *The overarching objective of this research is to develop IGC frameworks for hypersonic glide vehicles (HGVs) in lifting re-entry missions.*

A. Background

Re-entry guidance methods in the existing literature are largely based on simplified three-dimensional motion models of the vehicle and emphasize on designing bank angle commands to track specified flight profiles (e.g., angle of attack or altitude) or optimize a mission objective (e.g., range) [16, 20, 33]. For lifting bodies, the flight path angle profile can often be computed using the equilibrium or quasi-equilibrium glide constraint [16, 20, 33]. Also, feedback/compensation techniques can be introduced to accomplish certain mission objectives. For example, in Ref. [16], a compensation term based on the altitude rate tracking error is included into the commanded bank angle generator. Additionally, the reference altitude rate is shaped to alleviate 'phugoid'-like oscillations that may violate vehicle load constraints. Moreover, the bank angle profiles computed by these guidance laws might be non-smooth and/or discontinuous thus making tracking difficult for a controller. There are a small subset of guidance designs solely focused on the longitudinal motion of the vehicle [34–36]. One such design is given in Ref. [35], which involves computing a quasi-equilibrium glide trajectory in terms of flight path angle to operate at the maximum lift-to-drag ratio of the vehicle. The resulting trajectories exhibit poorly damped 'phugoid'-like oscillations. To address this, an angle of attack profile has been designed in Ref. [35] using the flight path angle error—which equals the deviation from a flight path angle profile corresponding to maximum lift-to-drag ratio—as a feedback term multiplied by a scalar gain. The numerical results in Ref. [35] indicate that a higher gain not only reduces the oscillations but also reduces the maximum heating rate and dynamic pressure, both of which are favorable for hypersonic flight.

When it comes to joint guidance and control architectures for HGVs, the state-of-the-art seems disjointed principally due to the independent development of guidance and control techniques without much consideration for synergy and integration. While the open existing literature provides a diverse set of guidance frameworks and algorithms suitable for HGVs in entry or re-entry missions, the body of literature on control frameworks for HGVs seem limited (see, for example, Refs. [10, 15]). Existing designs for hypersonic flight control are largely geared towards powered flight [4, 5, 8, 37] suitable for air-breathing cruise missions and cannot be trivially modified for gliding flight since thrust or fuel-to-air ratio is an integral part of these designs. In other words, thrust cannot simply be set to zero in these designs for gliding as that might render the closed-loop vehicle dynamics unstable. Furthermore, flight controls are largely based on the longitudinal motion of the vehicle, possibly under the assumption that the uncontrolled out-of-plane (i.e., lateral/directional) motion is stable or stabilizable, which might not hold in practice. All of these facets render majority of the existing control frameworks difficult to adapt for hypersonic re-entry missions and challenging to integrate with existing guidance techniques.

Although IGC architectures for HGVs could address the technical challenges outlined in the above discussion, availability of such methods remain limited in the open existing literature. Most of the existing frameworks for IGC (similar to the above-mentioned trend observed for existing hypersonic flight control designs) are geared towards hypersonic vehicles capable of powered flight [3, 20, 38–44]. Among these, earlier studies (see, for example, Refs. [3, 20, 38, 39]) focused on linearization-based techniques that could lead to unsatisfactory tracking performance and non-zero tracking errors, as indicated by the simulation results reported in Refs. [3, 38]. More recent works on hypersonic IGC can be found in Refs. [40–44], which often utilize principles of backstepping, dynamic surface control and finite-time stability. For example, Ref. [44] has recently introduced an IGC formulation where fuel-to-air ratio and elevator deflection are the control variables. The overall objective of the study in Ref. [44] is to drive velocity and altitude of the vehicle to their respective reference values while satisfying constraints on the fuel-to-air ratio magnitude. The guidance subsystem designs trajectories by incorporating these constraints and an adaptive backstepping approach is then applied for computing the control inputs for tracking. The simulation results in Ref. [44] show that although the constraints on the fuel-to-air ratio are satisfied, the controller initially commands a large elevator deflection (see Fig. 6 in Ref. [44]) as a large pitching moment—which is modeled as a linear function of the elevator deflection—is required for tracking. Adjusting numerical values of the control parameters might resolve this issue, but a more judicious approach would involve constraining the elevator deflections to be within physically allowable limits of the airframe. Unlike these above-mentioned studies on powered flight, an IGC framework for a generic HGV airframe/geometry has recently been proposed in Ref. [27]. The key contribution of that work lies in enabling IGC for a variety of hypersonic glide trajectories wherein the aerodynamic loads on the HGV are computed using high-fidelity computational fluid dynamics

simulations that account for the effects of control surface (i.e., stabilator) deflections. Furthermore, the flight controller in Ref. [27] is based on the principles of linear time-varying (LTV) model predictive control (MPC), and constraints on the HGV stabilator deflection are incorporated into the control synthesis.

B. Contribution

We propose a methodology for IGC of HGVs in re-entry missions executing a constant dynamic pressure glide under vertical quasi-steady equilibrium conditions. A simplified three-dimensional motion of a generic HGV geometry/airframe—introduced in Ref. [27]—with an emphasis on the longitudinal motion is adopted, wherein the aerodynamic loads are computed via modified Newtonian aerodynamics [45]. We consider stabilator deflection as the principal control input and treat the cosine of bank angle, which modulates the lift magnitude, as a second (pseudo) control. This is in contrast to the IGC methodology in Ref. [27] where stabilator deflection is the sole control input. The proposed guidance subsystem generalizes the method in Ref. [34] to capture the effects of stabilator deflection and angle of attack on the pitch rotational dynamics (more specifically, the pitching moment equilibrium or trim) of the vehicle. Inclusion of bank angle provides flexibility in satisfying the lift requirement for quasi-steady equilibrium and extends applicability of the guidance design which outputs reference signals in angle of attack, flight path angle, stabilator deflection, and cosine of bank angle for a given pair of altitude and speed of the HGV. The reference flight path angle is designed such that the error in dynamic pressure exponentially converges to zero, thereby enabling trajectories subject to initialization errors and disturbances to track the reference dynamic pressure. The LTV-MPC framework in Ref. [27] is adapted here to compute the commanded stabilator deflections and bank angles for tracking the reference signals generated by the guidance subsystem. This is achieved by solving a strictly convex quadratic program, which embeds box constraints on the deflection and bank angle magnitudes, at every sampling instant. Closed-loop simulations show that the proposed IGC framework successfully meets mission objectives despite non-zero trajectory initialization errors. Moreover, these simulation results demonstrate nominal robustness of the MPC design against plant-model mismatch [46, 47].

C. Organization

The remainder of the paper proceeds as follows: The preliminaries and problem formulation are detailed in Section II. Section III describes the proposed guidance design for constant dynamic pressure gliding and the LTV-MPC design for tracking is outlined in Section IV. Numerical results for a generic HGV geometry are included in Section V. Finally, the concluding remarks are summarized in Section VI.

II. Preliminaries

Basics of the problem formulation for the proposed IGC framework are provided in this section. This includes a simplified three-dimensional model of HGV motion and a modified Newtonian aerodynamics approach of calculating the aerodynamic forces and moments acting on the chosen HGV geometry.

A. HGV Motion Model

The simplified three-dimensional motion model described in Refs. [15, 18, 19, 48] is adopted for the current study. However, we have incorporated the HGV pitch rotational dynamics into the aforementioned model. Thus, the vehicle kinematics are given by

$$\begin{aligned} \dot{\chi}_d &= V\cos\gamma\cos\psi \\ \dot{\chi}_c &= V\cos\gamma\sin\psi \\ \dot{h} &= V\sin\gamma \end{aligned} \tag{1}$$

and the associated dynamics are described using the following set of ordinary differential equations

$$\begin{aligned} \dot{V} &= -\frac{D}{m_a} - g(h,V,\gamma)\sin\gamma \\ \dot{\alpha} &= q - \frac{L\cos\sigma}{m_a V} + \frac{g(h,V,\gamma)}{V}\cos\gamma \\ \dot{\gamma} &= \frac{L\cos\sigma}{m_a V} - \frac{g(h,V,\gamma)}{V}\cos\gamma \end{aligned} \tag{2}$$

$$\dot{q} = \frac{M_y}{I_y}$$
$$\dot{\psi} = \frac{L \sin\sigma}{m_a V}.$$

Here, χ_d and χ_c are the downrange and cross-range respectively, h is the altitude, V is the flight speed, α is the angle of attack, γ is the flight path angle, q is the pitch rate, σ is the bank angle, ψ is the heading angle, m_a is the HGV mass, and I_y is the moment of inertia about the HGV pitch axis. The aerodynamic loads—lift L, drag D and pitch moment M_y—are computed using modified Newtonian aerodynamics [45] under the assumption that the force and moment coefficients are primarily functions of the angle of attack α and stabilator deflection angle δ (see Section II.B). Also, the term $g(h, V, \gamma)$ denotes acceleration due to gravity which accounts for the centripetal effects of a spherical Earth of radius R_E and is modeled as [48]

$$g(h, V, \gamma) = \frac{\mu_E}{(R_E + h)^2} - \frac{V^2 \cos^2\gamma}{(R_E + h)} \tag{3}$$

where μ_E is the gravitational constant for Earth. Further, we assume an exponential atmospheric density model given by

$$\rho(h) = \rho_0 \exp(-a_h h) \tag{4}$$

where $\rho_0 = 1.225$ kg/m^3 and $a_h = 0.14/$ km. To simplify notations, we define $c_\sigma := \cos(\sigma)$, and rewrite the longitudinal dynamics in Eq. (2) in a compact form as

$$\dot{\mathbf{x}} = \mathbf{f}(\mathbf{x}, \mathbf{u}) \tag{5}$$

where $\mathbf{x} \in \mathbb{R}^4$ and $\mathbf{u} \in \mathbb{R}^2$ respectively denote the state and control input vectors, $\mathbf{f} : \mathbb{R}^4 \times \mathbb{R}^2 \to \mathbb{R}^4$ is the nonlinear function describing longitudinal dynamics, and these are given by

$$\mathbf{x} = \begin{bmatrix} V \\ \alpha \\ \gamma \\ q \end{bmatrix}, \ \mathbf{u} = \begin{bmatrix} \delta \\ c_\sigma \end{bmatrix}, \ \mathbf{f}(\mathbf{x}, \mathbf{u}) = \begin{bmatrix} -\frac{D}{m_a} - g(h, V, \gamma)\sin\gamma \\ q - \frac{L c_\sigma}{m_a V} + \frac{g(h,V,\gamma)}{V}\cos\gamma \\ \frac{L c_\sigma}{m_a V} - \frac{g(h,V,\gamma)}{V}\cos\gamma \\ \frac{M_y}{I_y} \end{bmatrix}.$$

Therefore, the cosine of bank angle c_σ is regarded as a (pseudo) control variable along with the stabilator deflection δ. While the longitudinal dynamics summarized above are used for designing the proposed IGC framework (see Sections III, IV), the effects of commanded bank angle on the lateral/directional motion have been captured through the heading angle variation described in Eq. (2). The heading angle variation, in turn, influences the kinematics in Eq. (1). These aspects of HGV motion have been included in the simulations (see Section V).

B. HGV Aerodynamics and Geometry

Modified Newtonian aerodynamics theory [45, 49] is used to generate lift, drag, and pitching moment loads for a given α and δ. The pressure coefficient C_p is defined as

$$C_p = \frac{p - p_\infty}{\frac{1}{2}\rho_\infty V_\infty^2}$$

where p and p_∞ respectively denote the surface pressure and free-stream static pressure, ρ_∞ denotes the free-stream density and V_∞ stands for the free-stream airspeed. Newtonian aerodynamics assumes that all of the momentum of a fluid stagnates in the normal direction of an exposed surface. Any surface that is not directly exposed to the flow only has a static pressure load applied. The result is that the pressure coefficient for the ith surface can be computed as an inner product between the surface's normal direction and the freestream flow direction using the following formula:

$$C_{p_i} = C_{p_0} \hat{\mathbf{V}}_\infty^{\mathrm{T}} \hat{\mathbf{n}}_i \tag{6}$$

where $\hat{\mathbf{V}}_\infty$ is a vector that describes the direction of the free-stream flow, $\hat{\mathbf{n}}_i$ is a unit vector that describes the normal direction of the ith surface, and $C_{p_0} = 2$ for traditional Newtonian aerodynamics [45]. However, for modified Newtonian aerodynamics, C_{p_0} is the pressure coefficient at a stagnation point behind a normal shock and depends on the Mach

number and specific heat ratio [45, Section 3.3]. As the Mach number approaches infinity, C_{p_0} can be calculated via the Rayleigh Pitot pressure formula for a given gas:

$$C_{p_0} \to \left(\frac{4}{\gamma_g + 1}\right)\left(\frac{(\gamma_g + 1)^2}{4\gamma_g}\right)^{\gamma_g/(\gamma_g - 1)}$$

where γ_g is the ratio of specific heats. Substituting $\gamma_g = 1.4$ for air in the above formula, the C_{p_0} for modified Newtonian aerodynamics is set to 1.839. Once the pressure coefficient is calculated for all of the surfaces around the vehicle, the resulting loads can be computed by summing the individual forces generated by those surfaces.

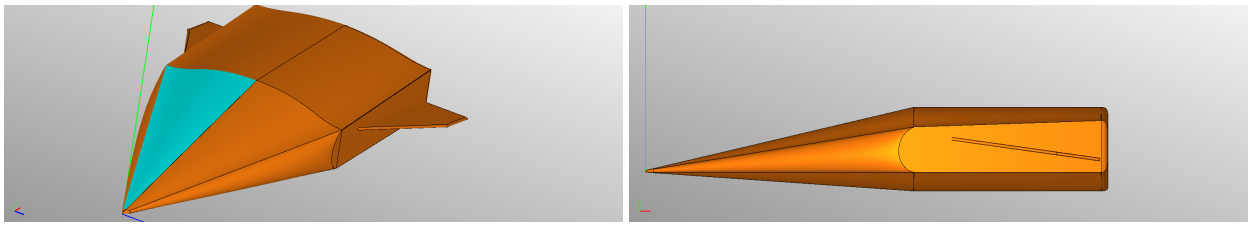

(a) **(b)**

Fig. 1 Geometry of the HGV [27].

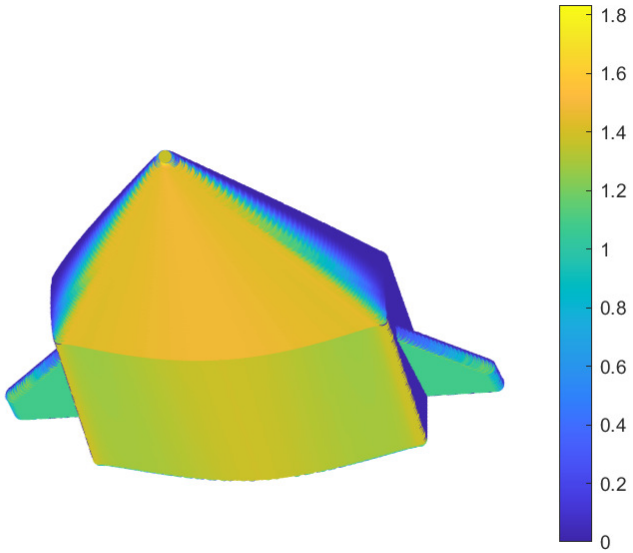

Fig. 2 HGV pressure coefficient distribution using modified Newtonian aerodynamics for $(\alpha, \delta) = (60, -10)$ deg.

This study focuses on the generic HGV geometry shown in Fig. 1, which has been recently developed at the University of Minnesota, Twin Cities [27]. The vehicle has two stabilators (i.e., the fins shown in Fig. 1) which are assumed be cojoined such that the corresponding angular deflections are the same about the vehicle's horizontal (front-to-aft) body axis. The relevant parameters for this vehicle geometry are

$$m_a = 1000 \text{ kg}, \; I_y = 247 \text{ kgm}^2, \; \bar{c} = 3.6 \text{ m}, \; S = 4.4 \text{ m}^2$$

where $\bar{c}$ and S stand for mean aerodynamic chord and reference area, respectively. The C_p distribution for the underside of the HGV is shown in Fig. 2 for $(\alpha, \delta) = (60, -10)$ deg, which approximately corresponds to the maximum lift

configuration. This C_p distribution was computed using modified Newtonian aerodynamics for 160,000 triangulated surfaces. As shown in Fig. 2, the aerodynamic load is generated primarily by the underside of the nose. Thus, by summing the resulting pressure distributions for a set of (α, δ) pairs, a database of aerodynamic coefficients has been generated for the aforementioned HGV geometry. These aerodynamic quantities are plotted in Fig. 3. We consider $\delta \in [-15, 15]$ deg for the database as those are the physical limits of the stabilator deflection for the airframe [27]. We define trim as $\dot{q} = 0$ or $M_y = 0$ for the HGV. The red lines in Fig. 3 denote $C_{M_y} = 0$ contours, highlighting the (α, δ) pairs for which the vehicle is at trim. We refer to these contours as "trim contours" which can be modified by shifting the center of gravity (CG) location of the vehicle.

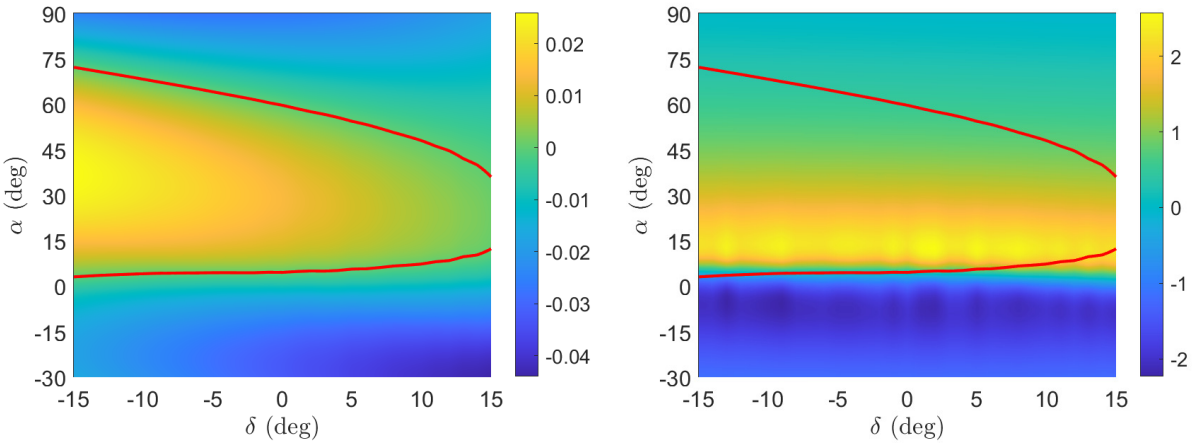

(a) Pitch moment coefficient (C_{M_y}) **(b) Lift-to-drag ratio (C_L/C_D)**

(c) Lift coefficient (C_L) **(d) Drag coefficient (C_D)**

Fig. 3 HGV aerodynamic load coefficients and lift-to-drag ratio using modified Newtonian aerodynamics for $\alpha \in [-30, 90]$ deg and $\delta \in [-15, 15]$ deg. The range of stabilator deflections δ here correspond to the physical limits of the HGV geometry [27]. The red lines are the trim contours satisfying $C_{M_y} = 0$ or $\dot{q} = 0$.

III. HGV Guidance Synthesis

This section elaborates guidance computations for a constant dynamic pressure, quasi-steady equilibrium glide trajectory. We suitably adapt the framework presented in Ref. [34] to incorporate pitch rotational dynamics and its coupling with (α, δ) for the generic HGV geometry considered in this paper. Computed trajectories simultaneously satisfy trim (defined by $\dot{q} = 0$ or $M_y = 0$) and lift requirements for quasi-steady equilibrium. The cosine of bank angle c_σ provides flexibility in satisfying the latter, which opens up the possibility of incorporating additional mission-related

criteria in the trajectory design. Moreover, the flight path angle design includes a term that drives the error in dynamic pressure (i.e., the offset from reference dynamic pressure) exponentially to zero. This feature not only allows a reference dynamic pressure to be specified and tracked, but also enables computation and optimization of trajectories capable of handling initialization errors, disturbances during flight etc. The following result summarizes the proposed guidance design in a generic setting as well as the regulatory assumptions associated with it.

Theorem 1 *Assume that the acceleration due to gravity takes a constant value denoted by g_0, the atmospheric density ρ is a function of altitude h, and the flight path angle γ abides by the small angle approximation so that* $\sin\gamma \approx \gamma$ *and* $\cos\gamma \approx 1$. *Let the flight path angle of the HGV be specified through*

$$\gamma = \frac{1}{\left(1 - \frac{V^2}{2g_0\rho(h)}\frac{d\rho}{dh}\right)}\left(-\frac{1}{\left(\frac{Lc_\sigma}{D}\right)} + \frac{e_\gamma \Delta p_d}{\rho(h) g_0 V}\right) \tag{7}$$

where e_γ is a positive weight and $\Delta p_d = p_d - p_{d_0}$ is the offset in dynamic pressure p_d from its constant reference value p_{d_0}. Also, let the lift force and bank angle satisfy the constraint $Lc_\sigma = m_a g_0$. Then, $\Delta\dot{p}_d = -e_\gamma \Delta p_d$, that is, the offset exponentially decreases to zero and the HGV flies a constant dynamic pressure glide trajectory under quasi-steady equilibrium conditions.

***Proof*:** Assume that the acceleration due to gravity is constant, denoted by g_0, and consider the specific energy $\mathcal{E} = h + 0.5V^2$. Its time derivative can be expressed as

$$\dot{\mathcal{E}} = \dot{h} + \frac{\dot{V}V}{g_0} = -\frac{DV}{m_a g_0} \tag{8}$$

where the last equality is obtained using $\dot{h}$ and $\dot{V}$ from the governing kinematics in Eq. (1) and dynamics in Eq. (2), respectively. For a small γ, the quasi-steady equilibrium glide condition, which requires $\dot{\gamma} = 0$ [16, 35], leads to $Lc_\sigma = m_a g_0$ as $\cos\gamma \approx 1$. Combining the $\dot{\mathcal{E}}$ expression in Eq. (8), the glide condition $Lc_\sigma = m_a g_0$ and the small angle approximation for γ, time derivative of downrange becomes

$$\dot{\chi}_d = V\cos\psi = -\frac{\dot{\mathcal{E}} m_a g_0}{D}\cos\psi = -\frac{\dot{\mathcal{E}} Lc_\sigma}{D}\cos\psi.$$

Thus, an infinitesimal change in the downrange can be expressed as

$$d\chi_d = -\frac{Lc_\sigma \cos\psi}{D} d\mathcal{E} = -\frac{Lc_\sigma \cos\psi}{D}\left(dh + \frac{V}{g_0}dV\right). \tag{9}$$

Now, differentiating the dynamic pressure $p_d = 0.5\rho(h)V^2$ with respect to time and setting the derivative equal to zero—such that the HGV glides at a constant dynamic pressure—yields

$$\begin{aligned} \dot{p}_d &= \rho(h)V\dot{V} + 0.5\dot{\rho}(h)V^2 \\ &= \rho(h)V\dot{V} + 0.5V^2\frac{d\rho}{dh}\dot{h} \\ &= 0 \end{aligned}$$

and therefore

$$\frac{V}{g_0}dV = -\frac{V^2}{2g_0\rho(h)}\frac{d\rho}{dh}dh. \tag{10}$$

Combining Eqs. (9) and (10), we obtain

$$\frac{d\chi_d}{dh} = -\frac{Lc_\sigma \cos\psi}{D}\left(1 - \frac{V^2}{2g_0\rho(h)}\frac{d\rho}{dh}\right).$$

Now, utilizing the governing kinematics in Eq. (1) for a small γ, we have $\frac{d\chi_d}{dh} = \frac{\cos\psi}{\gamma}$. Equating these two expressions of $\frac{d\chi_d}{dh}$ and solving for γ yields

$$\gamma = -\frac{(Lc_\sigma/D)^{-1}}{\left(1 - \frac{V^2}{2g_0\rho(h)}\frac{d\rho}{dh}\right)}.$$

This is similar to the expression provided in Ref. [34]. We intend to modify this design such that the error or offset in dynamic pressure $\Delta p_d = p_d - p_{d_0}$ converges to zero, and the vehicle tracks the specified, constant dynamic pressure p_{d_0}. To this end, the time derivative of Δp_d satisfies

$$\Delta\dot{p}_d = \dot{p}_d = \rho(h)V\dot{V} + 0.5\dot{\rho}(h)V^2 = -\frac{\rho(h)VD}{m_a} - \rho(h)V\gamma\left(g_0 - \frac{V^2}{2\rho(h)}\frac{d\rho}{dh}\right).$$

Then, choosing the flight path angle as in Eq. (7) results in

$$\Delta\dot{p}_d = \rho(h)Vg_0\left(\frac{D}{Lc_\sigma} - \frac{D}{mg_0}\right) - e_\gamma\Delta p_d$$

where the first term on the right hand side is equal to zero due to the quasi-steady equilibrium glide condition $Lc_\sigma = m_a g_0$. Therefore, we have $\Delta\dot{p}_d = -e_\gamma\Delta p_d$, which completes the proof. □

Remark 1 *To simplify the analysis involving specific energy, Theorem 1 is stated for a constant acceleration due to gravity by suppressing its variation with altitude, flight speed and flight path angle as modeled in Eq.* (3)*. Incorporating these effects into the analysis is beyond the scope of the current study in this paper and will be investigated in our future work. However, the proposed guidance synthesis (see Algorithm 1) combines Theorem 1 with the acceleration due to gravity model in Eq.* (3) *using a heuristic strategy that works well for the trajectories analyzed in this study (see Section V). The lift constraint for quasi-equilibrium glide in Theorem 1 can eliminate large phugoid-like oscillations in the altitude along re-entry trajectories [16, 20, 21, 35]. In this work, it is treated as a 'soft constraint'—consistent with existing literature on hypersonic re-entry guidance [16, 21, 34, 35]—such that $\dot{\gamma} \approx 0$ is allowed along the trajectories (see the simulation results in Section V). Finally, the proposed flight path angle design for an exponential atmospheric density model as in Eq.* (4) *becomes*

$$\gamma = \frac{1}{\left(1 + \frac{a_h V^2}{2g_0}\right)}\left(-\frac{1}{\left(\frac{Lc_\sigma}{D}\right)} + \frac{e_\gamma\Delta p_d}{\rho(h)g_0 V}\right), \tag{11}$$

which is obtained by substituting $\frac{d\rho}{dh} = -a_h\rho(h)$ into Eq. (7)*.*

Note that a larger e_γ would speed up convergence to the reference dynamic pressure but it should be chosen appropriately such that γ remains (approximately) a small angle throughout the flight, which would approximately maximize downrange [35]. Although the guidance law for flight path angle in Eq. (11) (or Eq. (7)) is derived under a constant acceleration due to gravity assumption, we can relax this assumption and employ the law for $g(h, V, \gamma = 0)$ where $g(h, V, \gamma)$ is as shown in Eq. (3). Thus, the HGV needs to operate such that $Lc_\sigma = m_a g(h, V, \gamma = 0)$ for quasi-steady equilibrium glide. This requirement could be satisfied with some $c_\sigma \leq 1$ if the HGV generates sufficient lift such that $L \geq m_a g(h, V, \gamma = 0)$. If the lift force isn't allowed to be modulated through c_σ, quasi-steady equilibrium would require $L = m_a g(h, V, \gamma = 0)$ which limits the feasible trajectory design space. Therefore, the term c_σ provides flexibility in trajectory design as the feasible design space satisfying $L \geq m_a g(h, V, \gamma = 0)$ should, in general, be larger compared to the more restrictive $L = m_a g(h, V, \gamma = 0)$ constraint. This, in principle, allows for additional mission-related criteria to be incorporated in the trajectory design. We also want trajectories satisfying trim, i.e., $\dot{q} = 0$ or $M_y = 0$. Thus, the computed glide trajectories need to satisfy the requirements of trim and quasi-steady equilibrium simultaneously. This generally involves searching over the design space, defined in terms of HGV states, control inputs, and geometry/airframe parameters (e.g., center of gravity or CG location, stabilator sizing, wing loading etc.), for feasible points satisfying both the requirements. Specifically, GC location of the vehicle plays a crucial role in determining if such feasible points exist for a given HGV airframe/geometry [36]. An exhaustive analysis to optimize the airframe/geometry parameters for mission-related requirements is possible but beyond the scope of current study.

In this work, it is assumed that the generic HGV geometry under consideration (see Section II.B) admits at least one feasible set of parameters such that the simultaneous quasi-equilibrium and trim requirements are met when operating close to the reference dynamic pressure. Also, as stated in Section II, we consider the aerodynamic force (lift and drag) and moment coefficients as functions of angle of attack α and stabilator deflection δ only. We focus on designing the HGV states (γ, α) and the control variables (δ, c_σ) in the proposed guidance synthesis whose feasibility is formalized—by essentially summarizing the above-mentioned aspects—in the following assumption.

Assumption 1 *The HGV geometry/airframe parameters and reference dynamic pressure are chosen such that the set*

$$\mathbb{F} = \{(\alpha, \delta, c_\sigma) : M_y = 0, Lc_\sigma = m_a g(h, V, \gamma = 0), (\delta, c_\sigma) \in \mathbb{U}\} \subset \mathbb{R}^3$$

with $g(h, V, \gamma)$ as in Eq. (3) is non-empty along vehicle trajectories satisfying $(h, V) \in [h_{\min}, h_{\max}] \times [V_{\min}, V_{\max}]$ for some $h_{\max} > h_{\min}$ and $V_{\max} > V_{\min}$. Here, $\mathbb{U} \subset \mathbb{R}^2$ denotes the set of admissible control inputs.

Assumption 1 underlines the importance of selecting the reference dynamic pressure in accordance with both the mission requirements and the aerodynamic capabilities of the airframe. The choice of reference dynamic pressure would be coupled with the range of lift coefficients satisfying trim and the admissible range of c_σ through the lift constraint for quasi-equilibrium gliding. Also, the values of $h_{\max}, h_{\min}, V_{\max}, V_{\min}$ would depend on the choice of reference dynamic pressure, while feasibility for $(h, V) \in [h_{\min}, h_{\max}] \times [V_{\min}, V_{\max}]$ would be important to account for trajectory dispersions.

Algorithm 1: HGV Guidance Synthesis

1 **Input:** HGV airframe/geometry parameters and reference dynamic pressure satisfying Assumption 1, set of admissible controls $\mathbb{U}$, altitude h and flight speed V such that $(h, V) \in [h_{\min}, h_{\max}] \times [V_{\min}, V_{\max}]$, and $e_\gamma > 0$.
2 Calculate the acceleration due to gravity $g(h, V, \gamma = 0)$ by setting $\gamma = 0$ in Eq. (3).
3 Compute the set $\mathbb{F} = \{(\alpha, \delta, c_\sigma) : M_y = 0, Lc_\sigma = m_a g(h, V, \gamma = 0), (\delta, c_\sigma) \in \mathbb{U}\}$.
4 Select a tuple $(\alpha, \delta, c_\sigma) \in \mathbb{F}$ according to some criteria.
5 Compute flight path angle γ using Eq. (7) or Eq. (11).
6 **Output:** $\gamma, \alpha, \delta, c_\sigma$

The proposed guidance synthesis is summarized in Algorithm 1 by embedding the conditions outlined in Assumption 1. For a given altitude and flight speed pair (h, V), the synthesis results in $(\gamma, \alpha, \delta, c_\sigma)$ for the associated glide trajectory. Since the set $\mathbb{F}$ is non-empty under Assumption 1, $(\alpha, \delta, c_\sigma) \in \mathbb{F}$ on line 4 in Algorithm 1 could be obtained by optimizing a mission-related objective or criteria. The reader is referred to Section V for the particular strategy adopted in the current study for selecting the $(\alpha, \delta, c_\sigma)$ tuple. Denoting the output of Algorithm 1 as $(\gamma_r, \alpha_r, \delta_r, c_{\sigma_r})$, the reference signals for tracking control can be specified as $\mathbf{x}_r = (V, \alpha_r, \gamma_r, 0)$ and $\mathbf{u}_r = (\delta_r, c_{\sigma_r})$, where the subscript '$r$' means 'reference'. Note that the reference pitch rate is zero, which could be replaced with a non-zero reference using trajectory information over some time window. As these reference signals are computed online for (h, V) pairs along the HGV closed-loop trajectory, the controller—which is tasked with tracking the reference signals—is inherently linked with it. The tracking control design used in this study is described next.

IV. LTV-MPC Design for Tracking: IGC of HGVs

The tracking control design—based on the principles LTV-MPC—is outlined in this section. The core methodology is adopted from Refs. [50, 51] with appropriate modifications to obtain a full-state feedback design for a time-varying system. Note that this design is also provided in Ref. [27] and included here for completeness. The LTV-MPC approach involves linearizing the longitudinal dynamics in Eq. (5) about a time-varying reference trajectory $\mathbf{x}_r(t)$ and reference control inputs $\mathbf{u}_r(t)$—obtained through the guidance synthesis (see Section III)—for the entire duration of the mission. We start by performing a Taylor series expansion of the nonlinear function about $(\mathbf{x}_r(t), \mathbf{u}_r(t))$, which leads to

$$\dot{\mathbf{x}}(t) = \mathbf{f}\left(\mathbf{x}_r(t), \mathbf{u}_r(t)\right) + \left.\frac{\partial \mathbf{f}}{\partial \mathbf{x}}\right|_{(\mathbf{x},\mathbf{u})=(\mathbf{x}_r(t),\mathbf{u}_r(t))} \left(\mathbf{x}(t) - \mathbf{x}_r(t)\right) + \left.\frac{\partial \mathbf{f}}{\partial \mathbf{u}}\right|_{(\mathbf{x},\mathbf{u})=(\mathbf{x}_r(t),\mathbf{u}_r(t))} \left(\mathbf{u}(t) - \mathbf{u}_r(t)\right) + \mathbf{w}(t) \tag{12}$$

where all the higher order terms are absorbed in $\mathbf{w}(t) := \mathbf{w}(\mathbf{x}(t), \mathbf{x}_r(t), \mathbf{u}(t), \mathbf{u}_r(t))$ and it can be treated as a time-varying disturbance. We introduce the following definitions to simplify notations in the ensuing analysis

$$\Delta\mathbf{x}(t) := \mathbf{x}(t) - \mathbf{x}_r(t),\ \Delta\mathbf{u}(t) := \mathbf{u}(t) - \mathbf{u}_r(t),\ \mathbf{A}(t) := \left.\frac{\partial \mathbf{f}}{\partial \mathbf{x}}\right|_{(\mathbf{x},\mathbf{u})=(\mathbf{x}_r(t),\mathbf{u}_r(t))},\ \mathbf{B}(t) := \left.\frac{\partial \mathbf{f}}{\partial \mathbf{u}}\right|_{(\mathbf{x},\mathbf{u})=(\mathbf{x}_r(t),\mathbf{u}_r(t))}.$$

Now, the linearized dynamics in Eq. (12) can be equivalently expressed as

$$\Delta\dot{\mathbf{x}} = \mathbf{A}(t)\Delta\mathbf{x} + \mathbf{B}(t)\Delta\mathbf{u} + \mathbf{w}(t). \tag{13}$$

Note that the linear time-varying system in Eq. (13) governs HGV longitudinal dynamics in a neighborhood of the time-varying reference trajectory and control inputs. The system in Eq. (13) can be discretized (e.g., using Euler discretization) and expressed as

$$\Delta\mathbf{x}(k+1) = \mathbf{A}_d(k)\Delta\mathbf{x}(k) + \mathbf{B}_d(k)\Delta\mathbf{u}(k) + \mathbf{w}(k) \tag{14}$$

where $k \in \mathbb{Z}_{\geq 0}$ are the sampling time steps or instances, with $\mathbb{Z}_{\geq 0}$ denoting the set of non-negative integers. Here, we take the discretization time-step equal to the sampling interval.

MPC is a finite-horizon optimal control strategy based on predicting future system behavior via a model of the system [52]. In this work, the LTV system in Eq. (14) serves as the model. However, we consider the disturbances to be identically zero in the prediction equations for the current MPC design. Also, the model matrices are held fixed over the MPC prediction horizon, which results in an optimization with reduced computational complexity [53, 54]. This linear time-invariant approach for prediction can be further justified by choosing sufficiently small values of the sampling interval and the number of time steps for prediction. The resulting prediction horizon (equal to the product of number of prediction time steps and sampling interval) would be short, whereby limiting the evolution of the underlying system over that timespan.

The prediction equations at a time-step k—obtained using Eq. (14) with $\mathbf{w}(k) = \mathbf{0}$ and model matrices $(\mathbf{A}_d(k), \mathbf{B}_d(k))$ held fixed at their values at k—are given in a compact form as

$$\Delta\mathbf{X}(k) = \mathbf{F}(k)\Delta\mathbf{x}(k) + \mathbf{H}(k)\Delta\mathbf{U}(k) \tag{15}$$

with

$$\Delta\mathbf{X}(k) = \begin{bmatrix} \Delta\mathbf{x}(k) \\ \Delta\mathbf{x}(k+1) \\ \Delta\mathbf{x}(k+2) \\ \cdot \\ \cdot \\ \cdot \\ \Delta\mathbf{x}(k+N-1) \end{bmatrix}, \ \Delta\mathbf{U}(k) = \begin{bmatrix} \Delta\mathbf{u}(k) \\ \Delta\mathbf{u}(k+1) \\ \Delta\mathbf{u}(k+2) \\ \cdot \\ \cdot \\ \cdot \\ \Delta\mathbf{u}(k+N-1) \end{bmatrix}, \mathbf{F}(k) = \begin{bmatrix} \mathbf{I}_4 \\ \mathbf{A}_d(k) \\ \mathbf{A}_d^2(k) \\ \cdot \\ \cdot \\ \cdot \\ \mathbf{A}_d^{N-1}(k) \end{bmatrix},$$

$$\mathbf{H}(k) = \begin{bmatrix} \mathbf{O} & \cdot & \cdot & \cdot & \cdot & \mathbf{O} \\ \mathbf{B}_d(k) & \cdot & \cdot & \cdot & \cdot & \mathbf{O} \\ \mathbf{A}_d(k)\mathbf{B}_d(k) & \mathbf{B}_d(k) & \cdot & \cdot & \cdot & \mathbf{O} \\ \mathbf{A}_d^2(k)\mathbf{B}_d(k) & \mathbf{A}_d(k)\mathbf{B}_d(k) & \mathbf{B}_d(k) & \cdot & \cdot & \mathbf{O} \\ \cdot & \cdot & \cdot & \cdot & \cdot & \cdot \\ \cdot & \cdot & \cdot & \cdot & \cdot & \cdot \\ \mathbf{A}_d^{N-2}(k)\mathbf{B}_d(k) & \mathbf{A}_d^{N-3}(k)\mathbf{B}_d(k) & \cdot & \cdot & \mathbf{B}_d(k) & \mathbf{O} \end{bmatrix}$$

where $\mathbf{I}_4$ is the 4×4 identity matrix and $\mathbf{O}$ denotes null matrices of appropriate dimensions, and N is the number of time steps associated with the prediction or control horizon. In other words, the prediction and control horizons are considered equal for the MPC formulation here. The terminal state perturbation is given by

$$\Delta\mathbf{x}(k+N) = \mathbf{A}_d^N(k)\Delta\mathbf{x}(k) + \bar{\mathbf{B}}_d(k)\Delta\mathbf{U}(k)$$

where $\bar{\mathbf{B}}_d(k) = \begin{bmatrix} \mathbf{A}_d^{N-1}(k)\mathbf{B}_d(k) & \mathbf{A}_d^{N-2}(k)\mathbf{B}_d(k) & \cdot & \cdot & \cdot & \mathbf{A}_d(k)\mathbf{B}_d(k) & \mathbf{B}_d(k) \end{bmatrix}$.

MPC allows the user to specify a cost (or objective) function which is typically minimized to calculate the optimal solution after each sampling interval. The cost function should be chosen such that minimizing it means that the control objectives (e.g., reference tracking, regulation etc.) have been satisfied with the least possible control effort. In this case, the control objective is regulation, i.e., we want to drive the predicted state perturbations in Eq. (15) to the origin, i.e., $\Delta\mathbf{X}(k) \to \mathbf{0}$. For the present formulation, we choose a cost function that penalizes the weighted norm of predicted state perturbations $\Delta\mathbf{X}(k)$ and the weighted norm of predicted control input perturbations $\Delta\mathbf{U}(k)$. We also incorporate a term penalizing the terminal state perturbation $\Delta\mathbf{x}(k+N)$. Therefore, the quadratic cost function for the LTV-MPC is

given by

$$
\begin{aligned}
&J\left(\Delta\mathbf{X}(k), \Delta\mathbf{x}(k+N), \Delta\mathbf{U}(k)\right) \\
&= \Delta\mathbf{x}^{\mathrm{T}}(k+N)\mathbf{Q}_f(k)\Delta\mathbf{x}(k+N) + \sum_{i=0}^{N-1} \Delta\mathbf{x}^{\mathrm{T}}(k+i)\mathbf{Q}\Delta\mathbf{x}(k+i) + \sum_{i=0}^{N-1} \Delta\mathbf{u}^{\mathrm{T}}(k+i)\mathbf{R}\Delta\mathbf{u}(k+i) \\
&= \Delta\mathbf{x}^{\mathrm{T}}(k+N)\mathbf{Q}_f(k)\Delta\mathbf{x}(k+N) + \Delta\mathbf{X}^{\mathrm{T}}(k)\bar{\mathbf{Q}}_N\Delta\mathbf{X}(k) + \Delta\mathbf{U}^{\mathrm{T}}(k)\bar{\mathbf{R}}_{\mathbf{N}}\Delta\mathbf{U}(k)
\end{aligned} \tag{16}
$$

where $\mathbf{Q}_f(k) \geq 0$ is time-dependent while $\bar{\mathbf{Q}}_N$ and $\bar{\mathbf{R}}_N$ are independent of time and given by

$$
\bar{\mathbf{Q}}_N = \mathrm{diag}\left(\mathbf{Q}, \mathbf{Q}, \ldots, \mathbf{Q}\right), \bar{\mathbf{R}}_N = \mathrm{diag}\left(\mathbf{R}, \mathbf{R}, \ldots, \mathbf{R}\right).
$$

Here, diag$(\cdot)$ means block-diagonal operation, $\mathbf{Q} \in \mathbb{R}^{4\times4}$ and $\mathbf{R} \in \mathbb{R}^{2\times2}$ are chosen such that $\mathbf{Q} \geq 0$ and $\mathbf{R} > 0$. The time-dependent matrix $\mathbf{Q}_f(k)$ is chosen based on the solution to the discrete-time Algebraic Riccati Equation, which is given by

$$
\mathbf{P} = \mathbf{A}_d^{\mathrm{T}}(k)\mathbf{P}\mathbf{A}_d(k) - \mathbf{A}_d^{\mathrm{T}}(k)\mathbf{P}\mathbf{B}_d(k)(\mathbf{R} + \mathbf{B}_d^{\mathrm{T}}(k)\mathbf{P}\mathbf{B}_d(k))^{-1}\mathbf{B}_d^{\mathrm{T}}(k)\mathbf{P}\mathbf{A}_d(k) + \mathbf{Q}.
$$

Upon solving the above equation, we set $\mathbf{Q}_f(k) = \mathbf{P}$. After substituting the expressions for $\Delta\mathbf{X}(k)$ and $\Delta\mathbf{x}(k+N)$ in Eq. (16), the cost function $J\left(\Delta\mathbf{X}(k), \Delta\mathbf{x}(k+N), \Delta\mathbf{U}(k)\right)$ becomes a quadratic in $(\Delta\mathbf{x}(k), \Delta\mathbf{U}(k))$ and can be expressed as

$$
\begin{aligned}
J(\Delta\mathbf{x}(k), \Delta\mathbf{U}(k)) = \Delta\mathbf{U}^{\mathrm{T}}(k)&\left[\mathbf{H}^{\mathrm{T}}(k)\bar{\mathbf{Q}}_N\mathbf{H}(k) + \bar{\mathbf{R}}_N + \bar{\mathbf{B}}_d^{\mathrm{T}}(k)\mathbf{Q}_f\bar{\mathbf{B}}_d(k)\right]\Delta\mathbf{U}(k) \\
&+ 2\left((\mathbf{F}(k)\Delta\mathbf{x}(k))^{\mathrm{T}}\bar{\mathbf{Q}}_N\mathbf{H}(k) + (\mathbf{A}_d^N(k)\Delta\mathbf{x}(k))^{\mathrm{T}}\mathbf{Q}_f\bar{\mathbf{B}}_d(k)\right)\Delta\mathbf{U}(k) \\
&+ (\mathbf{F}(k)\Delta\mathbf{x}(k))^{\mathrm{T}}\bar{\mathbf{Q}}_N(\mathbf{F}(k)\Delta\mathbf{x}(k)) + (\mathbf{A}_d^N(k)\Delta\mathbf{x}(k))^{\mathrm{T}}\mathbf{Q}_f(\mathbf{A}_d^N(k)\Delta\mathbf{x}(k)).
\end{aligned} \tag{17}
$$

We specify the input constraints as

$$
\mathbf{1}_N \otimes \Delta\mathbf{u}_{\min}(k) \leq \Delta\mathbf{U}(k) \leq \mathbf{1}_N \otimes \Delta\mathbf{u}_{\max}(k)
$$

where $\mathbf{1}_N$ stands for an N-dimensional vector of ones and $\otimes$ denotes the Kronecker product. Here, $\Delta\mathbf{u}_{\min}(k) = \mathbf{u}_{\min} - \mathbf{u}_r(k)$ and $\Delta\mathbf{u}_{\max}(k) = \mathbf{u}_{\max} - \mathbf{u}_r(k)$ with $\mathbf{u}_r(k)$ denoting the reference control input vector at some time-step k, and $\mathbf{u}_{\min}$ and $\mathbf{u}_{\max}$ respectively denote the minimum and maximum values of the control inputs.

Algorithm 2: HGV Integrated Guidance and Control Framework

Initialization: Given the mission time window $t \in [t_0, t_f]$, select a sampling interval Δt, set $t_k = t_0$ and $k = 0$. Choose the reference dynamic pressure, $\mathbf{Q}, \mathbf{R}, N, e_\gamma, \mathbf{u}_{\min}, \mathbf{u}_{\max}$.
while $t_k \leq t_f$ **do**
  Guidance Subsystem
    Given $(h(t_k), V(t_k))$, compute $\left(\alpha_r(t_k), \gamma_r(t_k), \delta_r(t_k), c_{\sigma_r}(t_k)\right)$ using Algorithm 1.
    Set $\mathbf{x}_r(t_k) = \begin{bmatrix} V(t_k) & \alpha_r(t_k) & \gamma_r(t_k) & 0 \end{bmatrix}^{\mathrm{T}}$, $\mathbf{u}_r(t_k) = \begin{bmatrix} \delta_r(t_k) & c_{\sigma_r}(t_k) \end{bmatrix}^{\mathrm{T}}$.
  Control Subsystem/Controller
    Generate continuous-time LTV model matrices $\mathbf{A}(t_k), \mathbf{B}(t_k)$ for $(\mathbf{x}_r(t_k), \mathbf{u}_r(t_k))$.
    Set $\Delta\mathbf{x}(k) = \mathbf{x}(t_k) - \mathbf{x}_r(t_k)$ and discretize $\mathbf{A}(t_k), \mathbf{B}(t_k)$ to obtain $\mathbf{A}_d(k), \mathbf{B}_d(k)$.
    Solve the SCQP in Eq. (18) to compute $\Delta\mathbf{u}^\star(k)$.
    Set $\mathbf{u}(t_k) = \mathbf{u}_r(t_k) + \Delta\mathbf{u}^\star(k)$.
  HGV Motion
    Integrate the kinematics in Eq. (1) and dynamics in Eq. (2) from t_k to $t_k + \Delta t$ using $\mathbf{u}(t_k)$.
    Set $t_k = t_k + \Delta t$, $k = k + 1$.

Therefore, the optimization problem for the LTV-MPC at each time-step $k \in \mathbb{Z}_{\geq 0}$ is given by

$$
\begin{aligned}
&\min_{\Delta\mathbf{U}(k)} \quad J\left(\Delta\mathbf{x}(k), \Delta\mathbf{U}(k)\right) \\
&\text{subject to} \quad \mathbf{1}_N \otimes \Delta\mathbf{u}_{\min}(k) \leq \Delta\mathbf{U}(k) \leq \mathbf{1}_N \otimes \Delta\mathbf{u}_{\max}(k)
\end{aligned} \tag{18}
$$

where $J\left(\Delta\mathbf{x}(k), \Delta\mathbf{U}(k)\right)$ is as shown in Eq. (17). The optimization in Eq. (18) is a strictly convex quadratic program (SCQP). Here, the constraints on $\Delta\mathbf{U}(k)$ are convex and the cost function $J\left(\Delta\mathbf{x}(k), \Delta\mathbf{U}(k)\right)$ is strictly convex in $\Delta\mathbf{U}(k)$ as the Hessian matrix satisfies

$$\left(\frac{\partial^2 J}{\partial \Delta\mathbf{U}^2(k)}\right) = \mathbf{H}^{\mathrm{T}}(k)\bar{\mathbf{Q}}_N\mathbf{H}(k) + \bar{\mathbf{R}}_N + \bar{\mathbf{B}}_d^{\mathrm{T}}(k)\mathbf{Q}_f\bar{\mathbf{B}}_d(k) > 0$$

since $\bar{\mathbf{R}}_N > 0$ by choice and the remaining two matrices are positive semi-definite. Therefore, the optimization problem in Eq. (18) admits a unique, global minimizer [55] for all time-steps k and can be computed efficiently using existing solvers. Let the minimizer at some time-step k be given by

$$\Delta\mathbf{U}^\star(k) = \left[(\Delta\mathbf{u}^\star)^{\mathrm{T}}(k) \quad (\Delta\mathbf{u}^\star)^{\mathrm{T}}(k+1) \quad (\Delta\mathbf{u}^\star)^{\mathrm{T}}(k+2) \quad \ldots \quad (\Delta\mathbf{u}^\star)^{\mathrm{T}}(k+N-1)\right]^{\mathrm{T}}.$$

Then, the control input vector at that time-step is chosen as $\mathbf{u}(k) = \mathbf{u}_r(k) + \Delta\mathbf{u}^\star(k)$.

Assume that $t \in [t_0, t_f]$ ($t_0 = 0$ without loss of generality) is the specified time window for the re-entry mission. Take Δt as the sampling interval for MPC and discretize the mission time window into time instances or steps separated by Δt time units. Now, consider the time instant corresponding to the k-th time-step, that is, $t_k = t_0 + k\Delta t$, and let the IGC module receive closed-loop trajectory information (including HGV altitude) for $t = t_k$. The guidance subsystem generates reference trajectory-controls pair $(\mathbf{x}_r(t_k), \mathbf{u}_r(t_k))$ using $(h(t_k), V(t_k))$ (see Algorithm 1), and passes on the reference values to the flight controller. The controller computes the LTV model matrices $\mathbf{A}(t_k), \mathbf{B}(t_k)$ corresponding to the reference pair $(\mathbf{x}_r(t_k), \mathbf{u}_r(t_k))$. Then, as described in this section, the model and the reference pair are utilized to compute the control inputs $\mathbf{u}(t_k)$ or $\mathbf{u}(k)$, i.e., the commanded δ and c_σ at time $t = t_k$ or time-step k. This procedure is repeated at every Δt time units over the entire mission, resulting in a feedback interconnection between the proposed guidance subsystem and flight controller. Therefore, HGV reference trajectories obtained via the proposed framework are coupled with the LTV-MPC design and the closed-loop flight controls acting on the vehicle. A summary of the proposed IGC framework is provided in Algorithm 2.

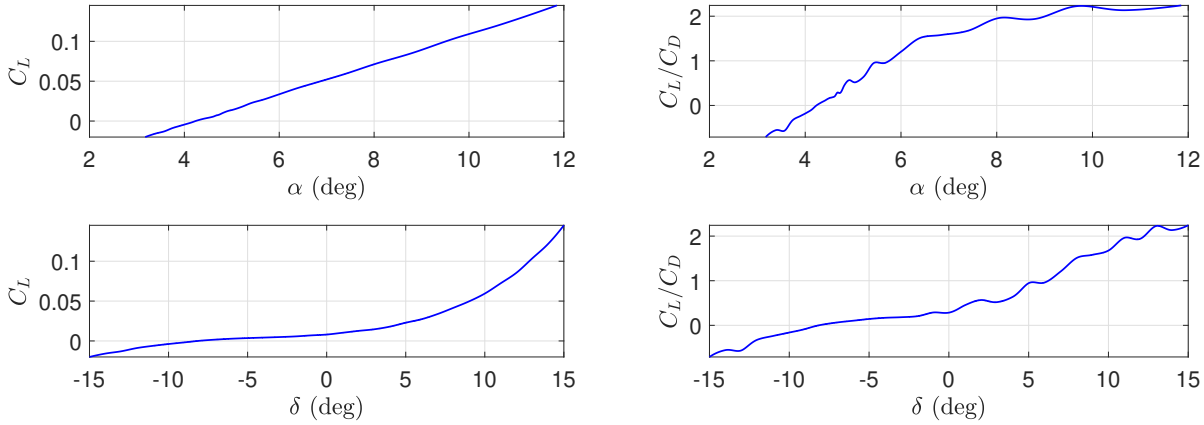

(a) Lift coefficient **(b) Lift-to-drag ratio**

Fig. 4 HGV lift coefficient and lift-to-drag ratio on the trim contour defined by $C_{M_y} = 0$ or $\dot{q} = 0$. These correspond to the low-α trim contour shown in Fig. 3.

V. Numerical Results

Simulation results of the proposed IGC framework for the generic HGV geometry and aerodynamic database described in Section II.B are provided in this section. First, we investigate feasibility of the proposed guidance synthesis and verify Assumption 1. To this end, we use fourth-order polynomials in (α, δ) to fit the trim contours shown in Fig. 3. Lift and drag coefficients associated with the fitted polynomials are obtained through local interpolation of the database. We utilize these lift coefficients to find $h_{\min}, h_{\max}, V_{\min}, V_{\max}$ such that Assumption 1 is satisfied for an admissible range

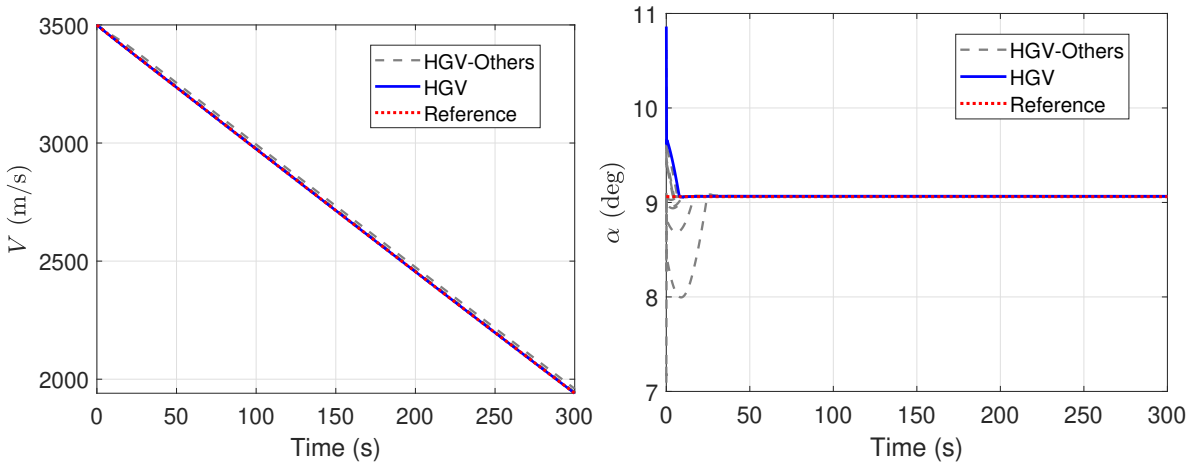

(a) Flight speed

(b) Angle of attack

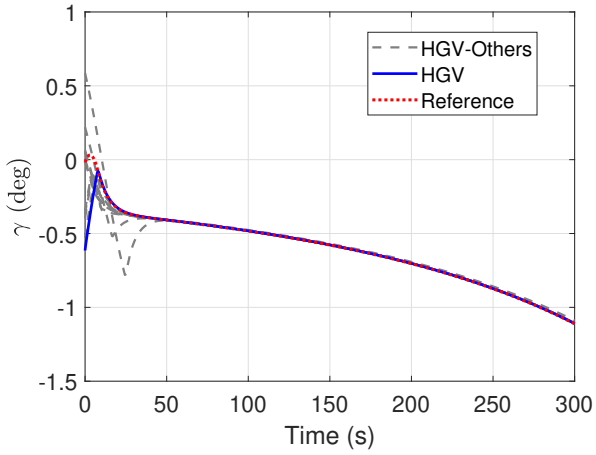

(c) Flight path angle

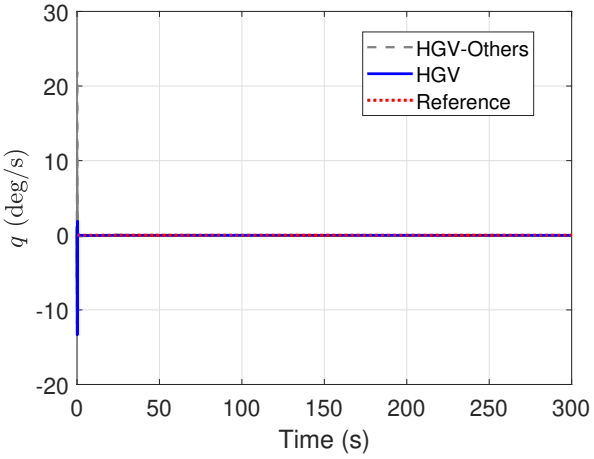

(d) Pitch rate

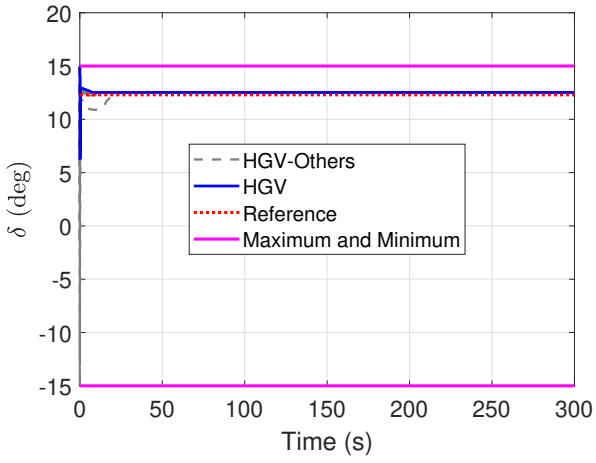

(e) Stabilator deflection

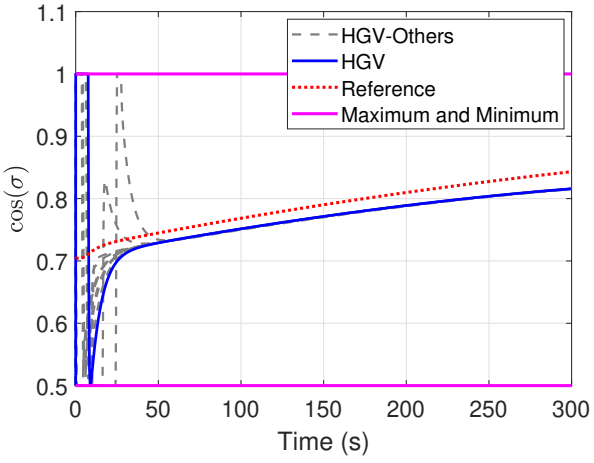

(f) Cosine of bank angle

Fig. 5 HGV closed-loop trajectories and control inputs. Reference signals here correspond to the trajectory and control inputs highlighted in blue. The trajectory in blue is initialized as in Eq. (20) with $\tau = 0.6$.

of c_σ, which would depend on the maximum allowable bank angle. For all the results in this section, we take the maximum bank angle equal to 60 deg, i.e., $c_\sigma \in [0.5, 1]$. Also, out of the two trim contours shown in Fig. 3, we choose

the low-α one as it corresponds to higher lift-to-drag ratio compared to the other contour. The lift coefficient (C_L) and lift-to-drag ratios on the chosen trim contour are respectively depicted in Figs. 4a and 4b, and the C_L here lies between -0.02 and 0.145. Then, satisfying Assumption 1 essentially boils down to finding zeros of the function

$$l(h, V, C_L, c_\sigma) = \frac{1}{2}\rho_0 \exp(-a_h h) V^2 S C_L c_\sigma - m_a \left(\frac{\mu_E}{(R_E + h)^2} - \frac{V^2}{(R_E + h)} \right)$$

for all values of $C_L \in (-0.02, 0.145)$, $c_\sigma \in [0.5, 1]$ and all (h, V) pairs corresponding to dynamic pressures that are close to the reference value specified for gliding. All the simulations in this section are initialized at $(h, V) = (40 \text{ km}, 3.5 \text{ km/s})$ and we select the reference dynamic pressure as 98% of its initial value. Now consider, for example, $(h_{\min}, h_{\max}) = (30, 45)$ km which yields $(V_{\min}, V_{\max}) = (1.72, 4.92)$ km/s for the reference dynamic pressure chosen. Quasi-steady equilibrium (i.e., $l(h, V, C_L, c_\sigma) = 0$) requires $0.0494 \leq C_L c_\sigma \leq 0.0774$, which is feasible for $C_L \in (-0.02, 0.145)$ and $c_\sigma \in [0.5, 1]$, thereby satisfying Assumption 1. Note that these are sample calculations and other values of $h_{\min}, h_{\max}, V_{\min}, V_{\max}$ satisfying Assumption 1 can be found. The key takeaway is that Assumption 1 holds for the reference dynamic pressure and the HGV geometry-related parameters (see Section II.B) chosen, rendering the proposed guidance synthesis in Algorithm 1 feasible for the simulations carried out here. With regards to Algorithm 1, we pick reference $(\alpha, \delta) = (9.1, 12.3)$ deg which would make the vehicle fly at 90% of the maximum lift-to-drag ratio on the trim contour (see Fig. 4b) with a lift coefficient $C_L = 0.0905$ (see Fig. 4a). The reference c_σ is then computed to satisfy the quasi-equilibrium glide constraint (i.e., $l(h, V, C_L, c_\sigma) = 0$) at a given pair of (h, V) along the trajectory.

Parameters related to the IGC framework (see Algorithm 2) are chosen as

$$\begin{aligned} &\Delta t = 10^{-2} \text{ s}, N = 10, \mathbf{u}_{\min} = (-15 \text{ deg}, 0.5)\,, \mathbf{u}_{\max} = (15 \text{ deg}, 1)\,, \\ &\mathbf{R} = 10^3 \mathbf{I}_2, \mathbf{Q} = \text{diag}\left(Q_V, Q_\alpha, Q_\gamma, Q_q\right), e_\gamma = 0.15 \end{aligned} \tag{19}$$

where $Q_V = 0.01$, $Q_\alpha = 10^7$, $Q_\gamma = 10^9$, and $Q_q = 10^3$, and $\mathbf{I}_2$ is the 2×2 identity matrix. Also, the time discretization is carried out through a zero-order hold and the SCQP in Eq. (18) is solved using MATLAB's QP solver 'quadprog'. The reference flight path angle computed via the guidance law (11) at the initial time $t = 0$ is $\gamma_r(0) = -0.015$ deg. The HGV is then randomly initialized around the reference state $\mathbf{x}_r(0) = \begin{bmatrix} V_r(0) & \alpha_r(0) & \gamma_r(0) & 0 \end{bmatrix}^{\mathrm{T}}$ with $V_r(0) = 3.5$ km/s and $\alpha_r(0) = 9.1$ deg as

$$\mathbf{x}(0) = \mathbf{x}_r(0) + \tau \begin{bmatrix} 0 & 3 \text{ deg} & -1 \text{ deg} & 2 \text{ deg/s} \end{bmatrix}^{\mathrm{T}} \tag{20}$$

where $\tau \in [-0.6, 0.6]$ is chosen randomly from an uniform distribution. No initial deviation in the flight speed is introduced as flight speed is not directly controlled or modulated, and it is allowed to decay as dictated by HGV dynamics along the trajectory. Time histories of closed-loop trajectories and control inputs are depicted in Fig. 5. The LTV-MPC controller successfully tracks the quasi-equilibrium reference trajectories despite initialization errors, while obeying the constraints on stabilator deflection and bank angle magnitudes. These randomly initialized simulations showcase nominal (i.e., inherent) robustness of the LTV-MPC design against plant-model mismatch [46, 47]. Theoretically assessing the robustness and convergence properties of the closed-loop error system associated with proposed IGC framework will be carried out in our future work. As shown in Fig. 6a, the reference dynamic pressure gets tracked approximately after $t = 50$ s for all the simulated trajectories and the transient oscillations initially are largely due to the tracking errors in the flight path angle (cf. Fig. 5c). We conclude that the requirements of the mission are therefore satisfied. However, the tracking in c_σ is biased, as shown in Fig. 5f. This is a consequence of the reference being generated through the quasi-equilibrium glide condition $\dot{\gamma} = 0$, while each trajectory actually requiring a small, negative $\dot{\gamma}$ (see Remark 1). While the MPC parameters here are tuned such that this requirement gets satisfied and the HGV successfully flies its mission, this discrepancy in $\dot{\gamma}$ will be investigated into more detail in our future work. Furthermore, the initial control input rates in these simulations are large and constraining the control input rates—along with the currently included magnitude constraints—will be a subject of future work as well.

Time histories of the kinematic states and the heading angle are shown in Fig. 6, where downrange, cross-range and heading angle are initialized at zero. The vehicle is observed to climb initially in an attempt to lower its dynamic pressure and converge close to the specified dynamic pressure which, as mentioned above, is 98% of the initial value. The altitude profiles do not exhibit phugoid-like oscillations [16, 35]—a benefit that likely stems from the quasi-steady equilibrium gliding condition despite the aforementioned biasing issue in c_σ. The downrange and cross-range values obtained here are of the order of 750 km and 250 km, respectively. The heading angles vary from zero to approximately 45 deg due to the non-zero bank angles commanded by the controller.

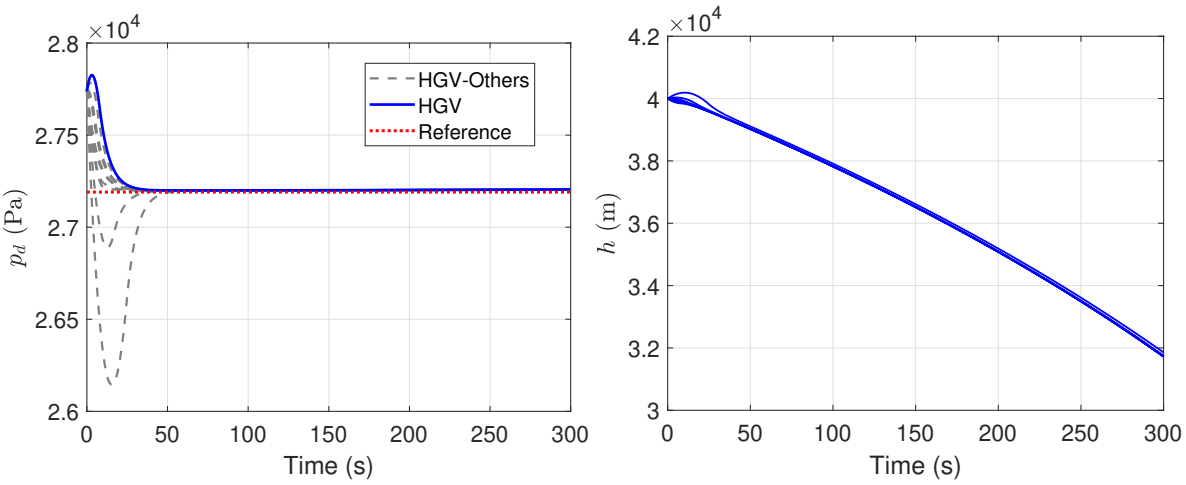

(a) Dynamic pressure

(b) Altitude

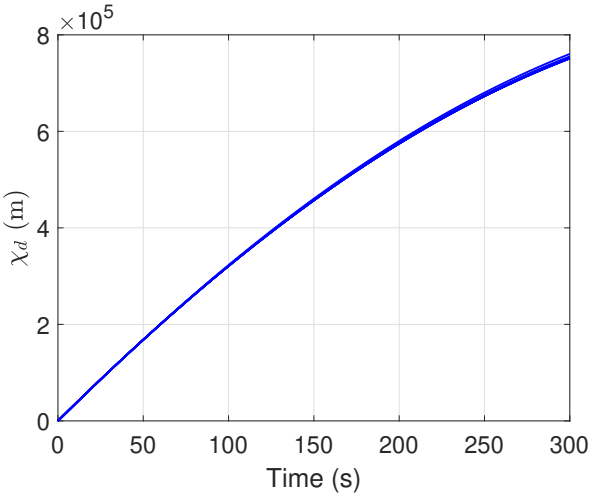

(c) Downrange

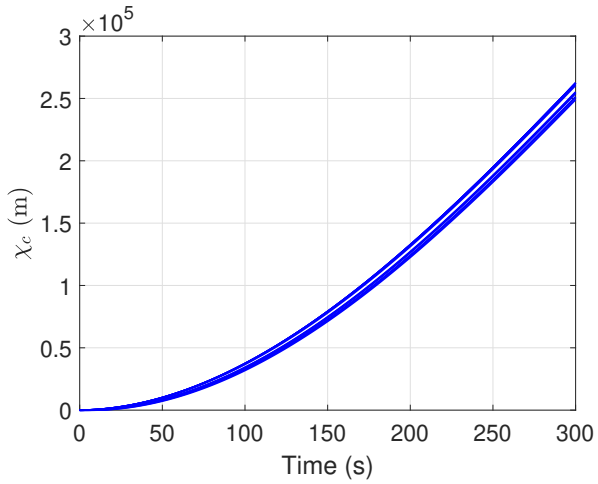

(d) Cross-range

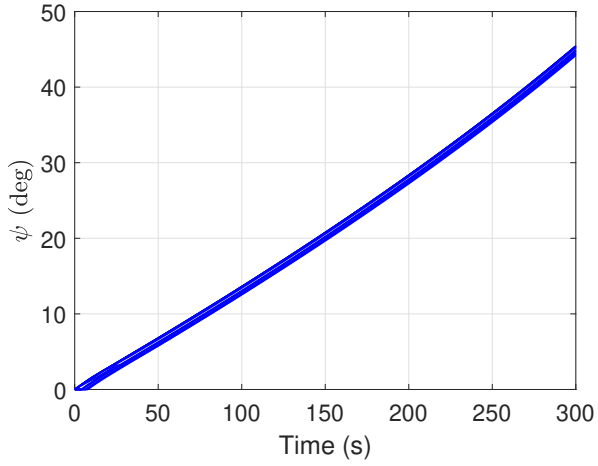

(e) Heading angle

Fig. 6 HGV dynamic pressures, kinematic states (altitude, cross-range, and downrange) and heading angles for the trajectories in Fig. 5.

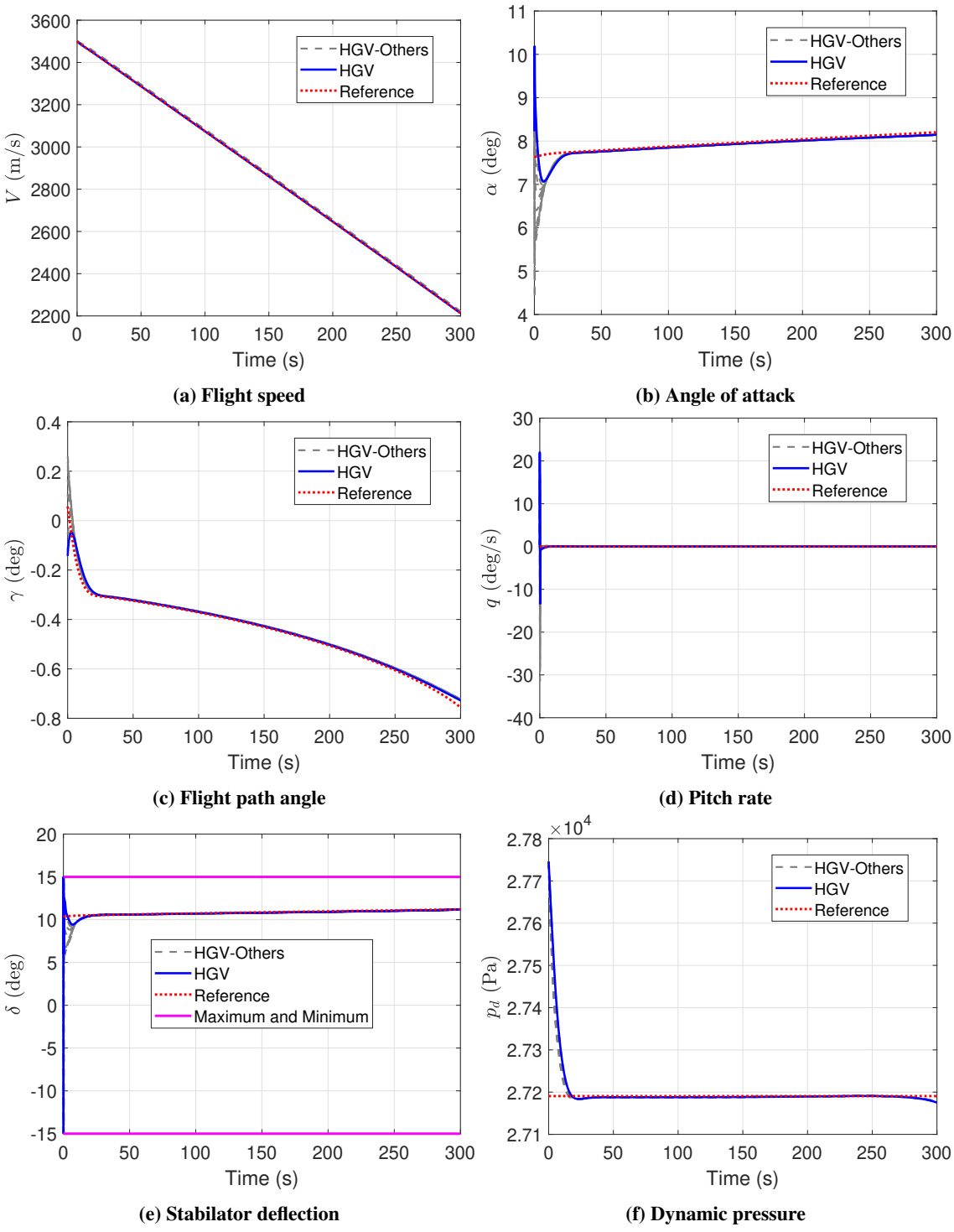

(a) Flight speed **(b) Angle of attack**

(c) Flight path angle **(d) Pitch rate**

(e) Stabilator deflection **(f) Dynamic pressure**

Fig. 7 HGV closed-loop trajectories, stabilator deflections, and dynamic pressures for the case where stabilator deflection is the only control input. Reference signals here correspond to the trajectory and stabilator deflection highlighted in blue. The trajectory in blue is initialized as in Eq. (20) with $\mathbf{x}_r(0) = \begin{bmatrix} 3.5 \text{ km/s} & 7.63 \text{ deg} & 0.057 \text{ deg} & 0 \end{bmatrix}^{\mathrm{T}}$ **and** $\tau = 0.2$.

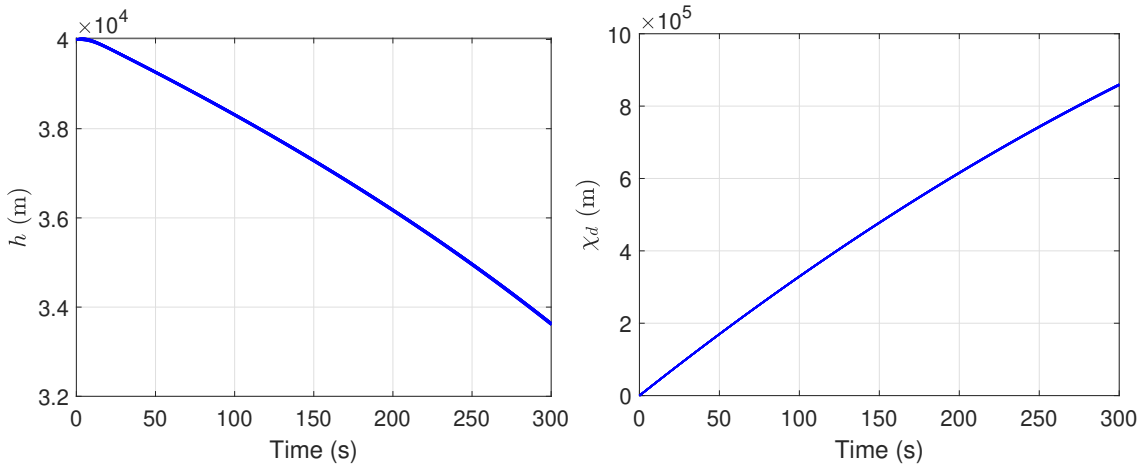

(a) Altitude **(b) Downrange**

Fig. 8 HGV kinematic states (altitude and downrange) for the trajectories in Fig. 7. This is the case where stabilator deflection is the only control input.

For comparison, another set of simulations is carried out by taking the stabilator deflection as the only control input and the bank angle is held constant at zero. The controller and guidance subsystem in Algorithm 2 are adjusted accordingly, while keeping the IGC parameters fixed at their values shown in Eq. (19). Also, the reference (α, δ) pairs for quasi-steady equilibrium gliding are different (see the discussion in Section III). The reference angle of attack and flight path angle at the initial time $t = 0$ are $(\alpha_r(0), \gamma_r(0)) = (7.63, 0.057)$ deg. Closed-loop simulations are carried out by setting the initial state as in Eq. (20) with the initial reference state $\mathbf{x}_r(0) = \begin{bmatrix} 3.5 \text{ km/s} & 7.63 \text{ deg} & 0.057 \text{ deg} & 0 \end{bmatrix}^{\mathrm{T}}$ and $\tau \in [-0.2, 0.2]$ randomly chosen from an uniform distribution. The time histories of closed-loop trajectories and stabilator deflections are shown in Fig. 7. The dynamic pressure profiles are shown in 7f and we can conclude that the mission objectives have been met in this set of simulations as well. But, the extent to which initial errors in the trajectory can be tolerated is much smaller here in contrast to the earlier case where both δ and c_σ were considered as control inputs. In fact, there is a three-fold reduction in the range of τ for which tracking becomes possible. This highlights the benefit of including bank angle as a (pseudo) control variable, while emphasizing on HGV motion in the longitudinal plane. Also, it is possible that the set of initial conditions for which closed-loop trajectories are tracked becomes smaller when c_σ is no longer considered as a control variable. A rigorous analysis is needed to substantiate this hypothesis and would be a part of our future work. The altitude and downrange profiles are shown in Fig. 8, with the downrange initialized at zero. The altitude profiles do not show phugoid-like oscillations and the downrange values here are of the order of 850 km, higher than the earlier case (compare Fig. 8b and Fig. 6c) as the heading angle remains fixed at zero.

We compute and compare heat fluxes and load factors for the two sets of trajectories simulated in this section. The load factor (n_L) and the Brandis-Johnston correlation [56, 57] for heat flux η are given by

$$n_L = \frac{\sqrt{L^2 + D^2}}{m_a}$$

$$\eta = 7.455 \times 10^{-9} r_n^{-0.52} \rho(h)^{0.4705} V^{3.089}$$

where r_n is the nose radius of the vehicle and η is expressed in terms of W/cm^2. The Van Driest model [49, 58] has also been employed for calculating the heat flux. Van Driest calculates the heat flux at a stagnation point by solving the boundary layer equations after a strong shock. Thus, the boundary layer edge conditions are computed using perfect gas shock theory. Once the post shock conditions are calculated for a given altitude and freestream velocity, heat flux is calculated via:

$$\eta = \kappa Pr^{-0.6} \sqrt{\rho_e \mu_e} \frac{1}{\sqrt{r_n}} \left(\frac{2(p_e - p_\infty)}{\rho_e} \right)^{1/4} (\nu_{aw} - \nu_w)$$

where $\kappa = 0.763$ for a sphere, Pr is the Prandtl number and is 0.72 for air, μ is the viscosity which is computed using the Sutherland's formula, and ν is the specific enthalpy. Here, the subscript e denote the boundary layer edge conditions,

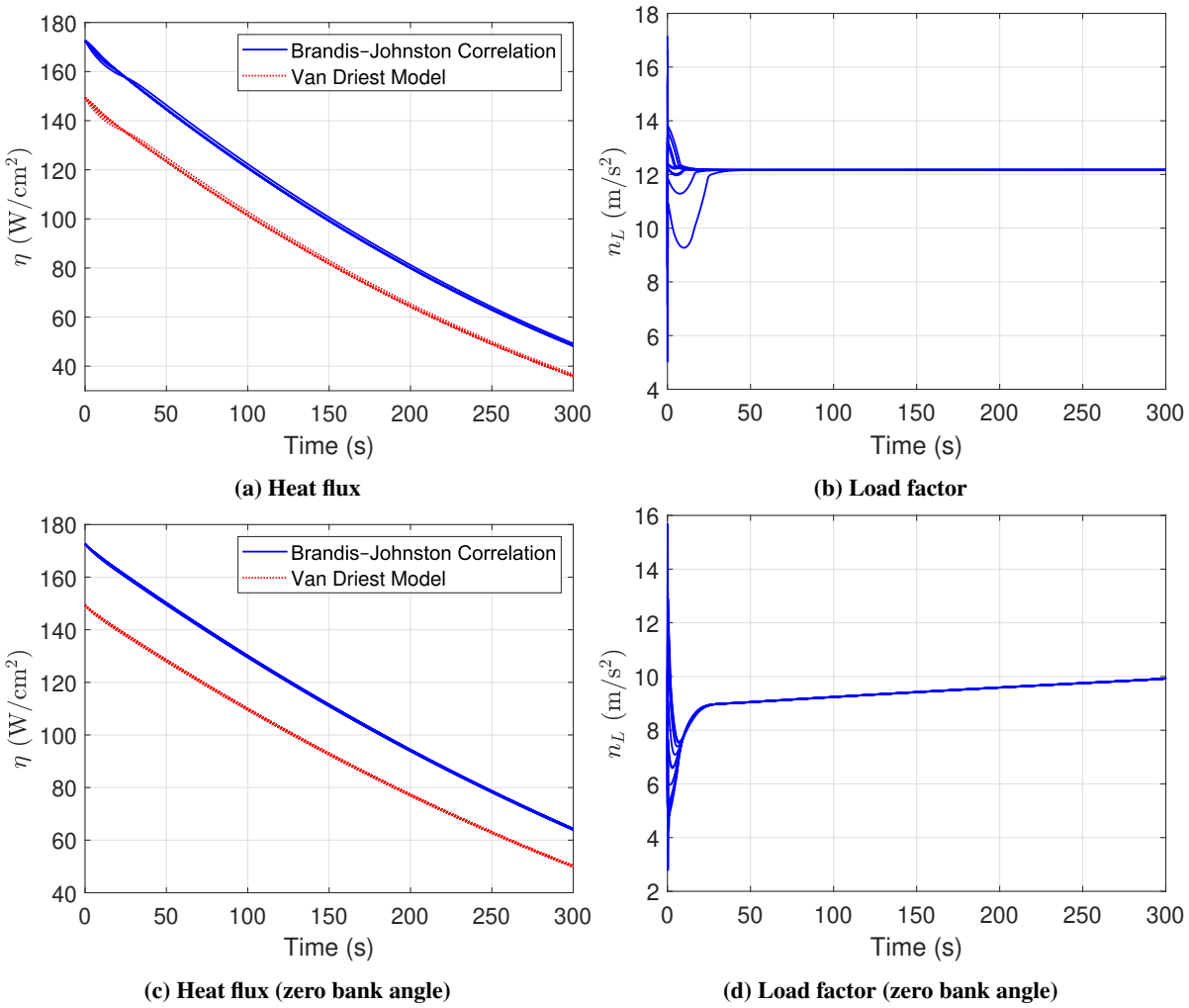

(a) Heat flux **(b) Load factor**

(c) Heat flux (zero bank angle) **(d) Load factor (zero bank angle)**

Fig. 9 HGV heat fluxes and load factors for the two sets of trajectories. The top row ((a), (b)) corresponds to the case where both stabilator deflection and cosine of bank angle are controls. The bottom row ((c), (d)) corresponds to the case where stabilator deflection is the only control input.

and the subscript w denote the wall conditions, and ν_{aw} corresponds to adiabatic wall conditions which is approximated as $\nu_{aw} = \nu_e + \frac{\sqrt{Pr}}{2}u_e^2$, where u_e is the boundary layer edge velocity. Also, ν_w assumes a constant wall or stagnation point temperature on the vehicle, which is assumed to be $T_w = 500$ K.

The load factor and heat flux results for the two sets of trajectories are shown in Fig. 9 where we have utilized $r_n = 0.1$ m as HGV nose radius. For trajectories where both δ and c_σ are control inputs, the load factors converge to a constant value after the initial oscillations (see Fig. 9b) as the vehicle starts operating at the reference $(\alpha, \delta) = (9.1, 12.3)$ deg and reference dynamic pressure, whereby the lift and drag forces acting on the vehicle become fixed. In contrast, the load factors in Fig. 9d, which correspond to the case where stabilator deflection δ is the only control input, slowly grow after the initial oscillations. As the HGV descends through the atmosphere, the acceleration due to gravity increases and the lift required for quasi-equilibrium gliding becomes higher. The slow growth in the load factors occur as the IGC framework accommodates the higher lift requirement. The heat fluxes for both sets of trajectories—as predicted by Brandis-Johnston correlation and Van Driest model—are shown in Figs. 9a, 9c. While the Van Driest model predicts lower values compared to the correlation formula, both methods indicate an approximately monotonic decrease in the heat flux with the vehicle descending and slowing down. Further, we observe that the heat flux decreases relatively quicker for trajectories with δ and c_σ as controls. This is caused by higher drag corresponding to those trajectories, which slows the HGV down quicker (compare Fig. 5a and Fig. 7a). The maximum allowable load

factor and heat flux for an airframe could become constraints in the guidance subsystem, and enforced via a choice of reference dynamic pressure and/or other constraints on HGV states. Our future work will involve investigating these aspects in the context of IGC for HGVs.

VI. Conclusions and Future Work

An IGC framework for constant dynamic pressure glide under vertical quasi-steady equilibrium conditions is proposed and investigated. The flight path angle guidance law generates glide trajectories convergent to the specified dynamic pressure despite initialization errors and other factors that might introduce an offset. Closed-loop simulations illustrate that the LTV-MPC design is inherently robust to plant-model mismatch and successfully flies the HGV subject to hard constraints on the control inputs. Furthermore, having only the stabilator deflection in the control channel leads to inferior convergence and tracking performance compared to the scenario where bank angle is considered as a second (pseudo) control variable along with stabilator deflection. Future work will focus on theoretically assessing this observation. Heat fluxes and load factors along the simulated closed-loop trajectories are analyzed. Embedding suitable constraints on these quantities in the IGC analysis and synthesis will be part of the future work.

Acknowledgments

This material is based upon work supported by the Air Force Office of Scientific Research under award number FA9550-22-1-0004.

References

[1] Lu, P., "What is guidance?" *Journal of Guidance, control, and Dynamics*, Vol. 44, No. 7, 2021, pp. 1237–1238.

[2] Lu, P., Shen, Z., Dukeman, G., and Hanson, J., "Entry guidance by trajectory regulation," *AIAA Guidance, Navigation, and Control Conference and Exhibit*, 2000, p. 3958.

[3] Lu, P., "Regulation about time-varying trajectories: precision entry guidance illustrated," *Journal of Guidance, Control, and Dynamics*, Vol. 22, No. 6, 1999, pp. 784–790.

[4] Xu, H., Mirmirani, M. D., and Ioannou, P. A., "Adaptive sliding mode control design for a hypersonic flight vehicle," *Journal of guidance, control, and dynamics*, Vol. 27, No. 5, 2004, pp. 829–838.

[5] Parker, J. T., Serrani, A., Yurkovich, S., Bolender, M. A., and Doman, D. B., "Control-oriented modeling of an air-breathing hypersonic vehicle," *Journal of Guidance, Control, and Dynamics*, Vol. 30, No. 3, 2007, pp. 856–869.

[6] Lu, P., "Predictor-corrector entry guidance for low-lifting vehicles," *Journal of Guidance, Control, and Dynamics*, Vol. 31, No. 4, 2008, pp. 1067–1075.

[7] Sigthorsson, D. O., Jankovsky, P., Serrani, A., Yurkovich, S., Bolender, M. A., and Doman, D. B., "Robust linear output feedback control of an airbreathing hypersonic vehicle," *Journal of guidance, control, and dynamics*, Vol. 31, No. 4, 2008, pp. 1052–1066.

[8] Fiorentini, L., Serrani, A., Bolender, M. A., and Doman, D. B., "Nonlinear robust adaptive control of flexible air-breathing hypersonic vehicles," *Journal of guidance, control, and dynamics*, Vol. 32, No. 2, 2009, pp. 402–417.

[9] Ataei, A., and Wang, Q., "Non-linear control of an uncertain hypersonic aircraft model using robust sum-of-squares method," *IET Control Theory & Applications*, Vol. 6, No. 2, 2012, pp. 203–215.

[10] Banerjee, S., Wang, Z., Baur, B., Holzapfel, F., Che, J., and Cao, C., "$\mathcal{L}1$ adaptive control augmentation for the longitudinal dynamics of a hypersonic glider," *Journal of Guidance, Control, and Dynamics*, Vol. 39, No. 2, 2016, pp. 275–291.

[11] Sagliano, M., Mooij, E., and Theil, S., "Adaptive disturbance-based high-order sliding-mode control for hypersonic-entry vehicles," *Journal of Guidance, Control, and Dynamics*, Vol. 40, No. 3, 2017, pp. 521–536.

[12] Sun, H., Yang, Z., and Zeng, J., "New tracking-control strategy for airbreathing hypersonic vehicles," *Journal of Guidance, Control, and Dynamics*, Vol. 36, No. 3, 2013, pp. 846–859.

[13] Lu, Y., "Disturbance observer-based backstepping control for hypersonic flight vehicles without use of measured flight path angle," *Chinese Journal of Aeronautics*, Vol. 34, No. 2, 2021, pp. 396–406.

[14] Sigthorsson, D., Serrani, A., Bolender, M., and Doman, D., "LPV control design for over-actuated hypersonic vehicles models," *AIAA guidance, navigation, and control conference*, 2009, p. 6280.

[15] Petersen, C., Baldwin, M., and Kolmanovsky, I., "Model predictive control guidance with extended command governor inner-loop flight control for hypersonic vehicles," *AIAA Guidance, Navigation, and Control (GNC) Conference*, 2013, p. 5028.

[16] Lu, P., "Entry guidance: a unified method," *Journal of Guidance, Control, and Dynamics*, Vol. 37, No. 3, 2014, pp. 713–728.

[17] Liu, X., Shen, Z., and Lu, P., "Entry trajectory optimization by second-order cone programming," *Journal of Guidance, Control, and Dynamics*, Vol. 39, No. 2, 2016, pp. 227–241.

[18] Shaffer, P., Ross, I., Oppenheimer, M., and Doman, D., "Optimal trajectory reconfiguration and retargeting for a reusable launch vehicle," *AIAA Guidance, Navigation, and Control Conference and Exhibit*, 2005, p. 6148.

[19] Shaffer, P. J., Ross, I. M., Oppenheimer, M. W., Doman, D. B., and Bollino, K. P., "Fault-Tolerant Optimal Trajectory Generationfor Reusable Launch Vehicles," *Journal of Guidance, Control, and Dynamics*, Vol. 30, No. 6, 2007, pp. 1794–1802.

[20] Shen, Z., and Lu, P., "Onboard generation of three-dimensional constrained entry trajectories," *Journal of Guidance, control, and Dynamics*, Vol. 26, No. 1, 2003, pp. 111–121.

[21] Xue, S., and Lu, P., "Constrained predictor-corrector entry guidance," *Journal of guidance, control, and dynamics*, Vol. 33, No. 4, 2010, pp. 1273–1281.

[22] Yu, W., and Chen, W., "Trajectory-Shaping Guidance with final speed and load factor constraints," *ISA transactions*, Vol. 56, 2015, pp. 42–52.

[23] Zang, L., Lin, D., Chen, S., Wang, H., and Ji, Y., "An on-line guidance algorithm for high L/D hypersonic reentry vehicles," *Aerospace Science and Technology*, Vol. 89, 2019, pp. 150–162.

[24] Mceowen, S., and Acikmese, B., "Hypersonic entry trajectory optimization via successive convexification with abstracted control," *AIAA SciTech 2022 Forum*, 2022, p. 0950.

[25] Mceowen, S., Kamath, A. G., Elango, P., Kim, T., Buckner, S. C., and Acikmese, B., "High-accuracy 3-DoF hypersonic reentry guidance via sequential convex programming," *AIAA scitech 2023 forum*, 2023, p. 0300.

[26] An, H., Xia, H., and Wang, C., "Barrier Lyapunov function-based adaptive control for hypersonic flight vehicles," *Nonlinear Dynamics*, Vol. 88, 2017, pp. 1833–1853.

[27] Williams, D., Bhattacharjee, D., Drayna, T. W., Bartkowicz, M., Hemati, M., and Candler, G. V., "Integrated Guidance and Control of Generic Hypersonic Glide Vehicles Using Computational Fluid Dynamics," *AIAA SCITECH 2025 Forum*, 2025, p. 0264.

[28] Coulter, B. G., Huang, D., and Wang, Z., "Geometric design of hypersonic vehicles for optimal mission performance with high-fidelity aerodynamic models," *Journal of Aircraft*, Vol. 60, No. 3, 2023, pp. 870–882.

[29] Decker, K., and Mavris, D. N., "A multidisciplinary analysis framework for the sizing and synthesis of hypersonic aerial systems," *AIAA SCITECH 2023 Forum*, 2023, p. 2365.

[30] Herrmann, E. G., Cox, A., and Mavris, D., "Multidisciplinary Design and Analysis of a Hypersonic Glide Vehicle With Trimmed Aerodynamics," *AIAA SCITECH 2025 Forum*, 2025, p. 1338.

[31] Santoso, F., Garratt, M. A., and Anavatti, S. G., "State-of-the-art integrated guidance and control systems in unmanned vehicles: A review," *IEEE Systems Journal*, Vol. 15, No. 3, 2020, pp. 3312–3323.

[32] Åström, K., *Introduction to stochastic control theory*, Mathematics in science and engineering, Vol. 70, Academic Press, United States, 1970.

[33] Lu, P., and Hanson, J. M., "Entry guidance for the X-33 vehicle," *Journal of Spacecraft and Rockets*, Vol. 35, No. 3, 1998, pp. 342–349.

[34] Kelley, H., Cliff, E., and Lutze, F., "Boost–glide range-optimal guidance," *Optimal Control Applications and Methods*, Vol. 3, No. 3, 1982, pp. 293–298.

[35] Yu, W., and Chen, W., "Guidance scheme for glide range maximization of a hypersonic vehicle," *AIAA Guidance, navigation, and control conference*, 2011, p. 6714.

[36] Jaeger, S. A., and Hemati, M. S., "Hypersonic Glide Vehicle Trajectory Design using Constrained Energy Maneuverability," 2025.

[37] Shin, J., "Adaptive dynamic surface control for a hypersonic aircraft using neural networks," *IEEE Transactions on Aerospace and Electronic Systems*, Vol. 53, No. 5, 2017, pp. 2277–2289.

[38] Roenneke, A. J., and Cornwell, P. J., "Trajectory control for a low-lift re-entry vehicle," *Journal of Guidance, Control, and Dynamics*, Vol. 16, No. 5, 1993, pp. 927–933.

[39] Schierman, J. D., Ward, D. G., Hull, J. R., Gandhi, N., Oppenheimer, M., and Doman, D. B., "Integrated adaptive guidance and control for re-entry vehicles with flight test results," *Journal of Guidance, Control, and Dynamics*, Vol. 27, No. 6, 2004, pp. 975–988.

[40] Dong, M., Xu, X., and Xie, F., "Constrained Integrated Guidance and Control Scheme for Strap-Down Hypersonic Flight Vehicles with Partial Measurement and Unmatched Uncertainties," *Aerospace*, Vol. 9, No. 12, 2022, p. 840.

[41] Wang, J., Liu, L., Zhao, T., and Tang, G., "Integrated guidance and control for hypersonic vehicles in dive phase with multiple constraints," *Aerospace Science and Technology*, Vol. 53, 2016, pp. 103–115.

[42] Zhang, D., Ma, P., Wang, S., and Chao, T., "Multi-constraints adaptive finite-time integrated guidance and control design," *Aerospace Science and Technology*, Vol. 107, 2020, p. 106334.

[43] Zhenyu, C., Jianguo, G., Bin, Z., Zongyi, G., and Xiaodong, L., "Finite-time integrated guidance and control system for hypersonic vehicles," *Transactions of the Institute of Measurement and Control*, Vol. 43, No. 4, 2021, pp. 842–853.

[44] Shou, Y., Yan, T., Xu, B., and Sun, F., "Integrated guidance and control of hypersonic flight vehicle with coordinated mission requirement and input constraint," *International Journal of Robust and Nonlinear Control*, Vol. 33, No. 7, 2023, pp. 4262–4280.

[45] Anderson, J. D., *Hypersonics and High-Temperature Gas Dynamics*, 3rd ed., AIAA Education Series, AIAA, 2007, Chap. 3, pp. 54–63.

[46] Kuntz, S. J., and Rawlings, J. B., "Offset-free model predictive control: stability under plant-model mismatch," , 2024. URL `https://arxiv.org/abs/2412.08104`.

[47] Kuntz, S. J., and Rawlings, J. B., "Beyond inherent robustness: strong stability of MPC despite plant-model mismatch," , 2025. URL `https://arxiv.org/abs/2411.15452`.

[48] Wiesel, W. E., *Spaceflight Dynamics*, McGraw-Hill Companies Inc., 1997.

[49] Candler, G., *Hypersonic Aerodynamics Course Notes*, University of Minnesota, 2024.

[50] Ru, P., and Subbarao, K., "Nonlinear model predictive control for unmanned aerial vehicles," *Aerospace*, Vol. 4, No. 2, 2017.

[51] Subbarao, K., Tule, C., and Ru, P., "Nonlinear model predictive control applied to trajectory tracking for unmanned aerial vehicles," *Aiaa atmospheric flight mechanics conference*, 2015, p. 2857.

[52] Rawlings, J. B., Mayne, D. Q., Diehl, M., et al., *Model predictive control: theory, computation, and design*, Vol. 2, Nob Hill Publishing Madison, WI, 2017.

[53] Falcone, P., Tufo, M., Borrelli, F., Asgari, J., and Tseng, H. E., "A linear time varying model predictive control approach to the integrated vehicle dynamics control problem in autonomous systems," *2007 46th IEEE conference on decision and control*, IEEE, 2007, pp. 2980–2985.

[54] Falcone, P., Borrelli, F., Tseng, H. E., Asgari, J., and Hrovat, D., "Linear time-varying model predictive control and its application to active steering systems: Stability analysis and experimental validation," *International Journal of Robust and Nonlinear Control: IFAC-Affiliated Journal*, Vol. 18, No. 8, 2008, pp. 862–875.

[55] Boyd, S., and Vandenberghe, L., *Convex Optimization*, Cambridge University Press, 2004.

[56] Brandis, A. M., and Johnston, C. O., "Characterization of stagnation-point heat flux for earth entry," *45th AIAA Plasmadynamics and Lasers Conference*, 2014, p. 2374.

[57] Rataczak, J. A., Chaudhry, R. S., McMahon, J. W., and Boyd, I. D., "Investigation of Surface-Catalycity Effects on Hypersonic Glide Vehicle Trajectory Optimization," *Journal of Spacecraft and Rockets*, Vol. 61, No. 4, 2024, pp. 1019–1031.

[58] Van Driest, E. R., *The problem of aerodynamic heating*, Institute of the Aeronautical Sciences Los Angeles, 1956.